



Numerical analysis of dynamics between debris flows and wave propagation using multi-layer shallow water equations

Seungjun Lee¹, Hyunuk An², Minseok Kim¹, Taeun Kang³

¹Geologic Hazards Division, Korea Institute of Geoscience and Mineral Resources, Daejeon, 34132, Republic of Korea

5 ²Department of Agricultural and Rural Engineering, Chungnam National University, Daejeon, 34134, Republic of Korea

³Division for Integrated Water Management, Korea Environment Institute, Sejong, 30147, Republic of Korea

Correspondence to: Hyunuk An (hyunuk@cnu.ac.kr)

Abstract. Landslides and debris flows are significant disasters that frequently occur on hillslopes, often resulting in casualties and property damage when they take place near residential areas. Specifically, in regions with dams or reservoirs, landslides and debris flows can raise the top of dead storage, reducing the effective storage capacity of these facilities. Additionally, debris flows entering reservoirs can generate tsunami-type waves, potentially leading to overflow-induced flooding and the collapse of hydraulic structures. Numerical modeling has been widely employed to mitigate such disasters. However, most studies utilized three-dimensional hydrodynamics or smoothed particle hydrodynamics, focusing primarily on laboratory-scale events without considering critical processes such as erosion, entrainment, and deposition. These processes are essential for accurately simulating debris flow dynamics. To address these limitations, this study developed a multi-layer dynamics simulation model based on shallow water equations that consider erosion, entrainment, and deposition mechanics, enabling the analysis of field-scale events. The model's performance was validated through theoretical and laboratory experiments. The 2020 Sanyang Reservoir collapse event in South Korea was selected as a case study to evaluate the model's applicability. Scenario-based analyses were conducted, considering debris flow characteristics and reservoir water level conditions, to explore various potential outcomes. The results highlighted the correlation between debris flow momentum and wave scale, with the maximum momentum of the debris flow identified as a strong predictor of the wave's magnitude.

1 Introduction

Landslides and debris flows are representative geohazards that occur in both natural and artificial slopes, causing significant changes in the landscape. Generally, landslides refer to ground collapse (Terzaghi, 1950), and debris flows refer to fluid-like movement through the liquefaction of collapsed soil and rock (Takahashi, 1978). Although different factors, such as earthquakes, volcanic activity, heavy rainfall, typhoons, and snow melting trigger landslide–debris flow events, rainfall is the most dominant (Wieczorek, 1996; Wieczorek and Glade, 2005; Kim et al., 2021). When landslides and debris flows occur near residential areas or roads, they cause casualties and property damage and require substantial staffing and resources for recovery. Therefore, most governments focus on developing and implementing disaster prevention and conducting research and development projects in densely populated cities that are prone to disasters. Consequently, several researchers have actively



conducted monitoring (Iverson et al., 2011; Zhou et al., 2019), as well as experimental (Oguchi and Oguchi, 2004; Blasone et al., 2014; Hürlimann et al., 2014; Gao et al., 2017; Lyu et al., 2022) and numerical modeling (Denlinger and Iverson, 2001; Pitman et al., 2003; An et al., 2019; Lee et al., 2022a) to analyze landslide–debris flows in urban areas. In addition, numerous studies have been conducted based on the above analyses to mitigate damage through structural (Shrestha et al., 2012; Chen et al., 2019; Shen et al., 2019; Choi et al., 2021) and non-structural (Zhao et al., 2022) approaches to develop effective response strategies.

However, landslides and debris flows occur in not only urban areas but also mountainous regions with extensive mountain ranges, rivers, and coastal areas. Moreover, areas with large and widespread mountain ranges often have numerous reservoirs and dams, and landslides and debris flows originating from natural slopes in the dam/reservoir basin can affect these structures (Lee et al., 2023). For instance, the landslide–debris flow event on March 22, 1959, in the Pontesei Dam basin resulted in the influx of debris into the reservoir, causing a tsunami and one fatality. Similarly, the landslide–debris flow event in the Vajont Dam basin on October 9, 1963, led to a tsunami that killed nearly 2,000 people (Schnitter and Weber, 1964; Slingerland and Voight, 1979). Another example is the landslide–debris flow event on July 14, 2003, in the Gorges Reservoir basin, which also generated a tsunami and caused 24 fatalities (Wang et al., 2004). Landslides and debris flows occurring near dams/reservoirs can not only cause performance degradation of the facilities by raising the top of dead storage but also tsunami-type waves by magnitude sediment flowing into the reservoir (Lee et al., 2023). Therefore, studies on landslides and debris flows in watersheds with dams or reservoirs that are different from those in urban areas are essential for effectively managing dams and reservoirs (ICOLD, 2009). Despite the potential for large-scale complex hazards caused by landslide–debris flow events in dam/reservoir basins, they have received less attention and research than urban areas. Landslide–debris flows occurring not only in dams and reservoirs but also in riverine environments can restrict the flow of rivers or induce eutrophication, thus threatening aquatic ecosystems (Shaffer and Parks, 1994). Similarly, landslide–debris flows near the coast can damage economically valuable coastal areas or cause red tide (Kim et al., 2009). Given the multidimensional significance of sediment influx into water systems, sufficient research is essential. However, considering and analyzing the dynamics of two contrasting materials is highly complex, requiring prior research on the impact of landslide–debris flow events on a stable hydrological regime. To understand these phenomena, several experiments (Heinrich, 1992; Rzedkiewicz et al., 1997; Heller and Spinneken, 2015; Mulligan and Take, 2017; Bullard et al., 2019; de Lange et al., 2020) and numerical analyses have been conducted (Imamura et al., 2001; Abadie et al., 2010; Pudasaini, 2014; Franci et al., 2020; Dai et al., 2021).

Heinrich (1992) and Rzedkiewicz et al. (1997) conducted experiments and numerical analyses on submerged soil collapse. The former assumed that the soil was a rigid body and addressed wave propagation. The latter complemented Heinrich's research by analyzing soil as cohesive sediment instead of a rigid body. Bullard et al. (2019) and de Lange et al. (2020) conducted experiments to analyze the behavior of a wave when debris flows inflow to water along slopes. Bullard et al. (2019) assessed the interaction between debris flow and free water surface, but they used water rather than soil to simulate the debris flow. de Lange et al. (2020) complemented Bullard et al.'s experiment by using soil to simulate the debris flow. However, most of these experiments focused on the behavior of landslides, debris flows, and wave dynamics based on monitoring data.



65 Parallel numerical modeling analysis is necessary to ensure applicability in terms of prediction and response. Accordingly, Pudasaini (2014), Franci et al. (2020), Dai et al. (2021), and Guan and Shi (2023) simulated the interaction between debris flow and water using a two-layer technique, three-dimensional (3D) hydrodynamics, particle method to analyze this phenomenon physically. Pudasaini (2014) interpreted the phenomenon based on full physical mechanics. However, their simulation results were not validated, and the developed two-layer numerical model was primarily designed for analyzing the

70 liquefaction process of debris flows, i.e., multi-phase. As a result, additional research and improvements are needed to address the interaction mechanisms between debris flows and water. Dai et al. (2021), and Guan and Shi (2023) used the smoothed particle hydrodynamics (SPH) technique to analyze this phenomenon and validated the accuracy of the simulation results; however, the validation was only performed for specific situations (assuming rigid body behavior of the sediment). In addition, the SPH technique requires further validation due to accuracy variations influenced by the size, shape, and number of particles

75 used in simulations. To achieve comparable simulation accuracy, SPH generally demands greater computational time than grid-based hydrodynamics (Han et al., 2020; Guan and Shi, 2023). Franci et al. (2020) and Franco et al. (2021) simulated soil inflow using the particle finite element method (PFEM) and Flow3D, respectively. Although these particle and 3D methods simulate with high accuracy, their high computational requirements pose challenges for field scale analyses (Ouyang et al., 2013). Therefore, most research on numerical modeling has focused on simulating laboratory experiments. Although some

80 studies address field-scale events, they typically use a mean element size greater than 10 m or a grid resolution exceeding 20 m (Pudasaini, 2014; Franci et al., 2020; Dai et al., 2021; Guan and Shi, 2023), which are considered too coarse to accurately analyze debris flow (Stolz and Huggel, 2008; Horton et al., 2013; Qiu et al., 2022). Moreover, existing studies have often overlooked key processes of debris flows, such as erosion, entrainment, and deposition. These processes significantly influence the flow volume and momentum of debris flows (VanDine and Bovis, 2002; Hungr et al., 2005; Iverson et al., 2011; Pudasaini

85 and Krautblatter, 2021), and prior research has demonstrated that the wave magnitude induced by debris flows is directly proportional to their volume and momentum (de Lange et al., 2020; Dai et al., 2023). Therefore, to analyze complex hazards caused by landslide–debris flow, it is essential to account for erosion, entrainment, and deposition processes. However, numerical models capable of comprehensively incorporating these processes for analyzing complex hazards remain limited. Therefore, this study developed a numerical model, that is, a multi-layer flow analysis model based on the hyperbolic form of

90 the shallow water equations, to analyze landslide–debris flow events in a dam/reservoir basin (field-scale events). Moreover, the developed numerical model was designed to simulate erosion, entrainment, and deposition processes. The model ensures numerical stability by discretizing it using the finite volume method (FVM). To achieve mathematical and physical stability, the upwinding dispersive correction hydrostatic reconstruction (UDCHR) scheme proposed by Bouchut and Zeitlin (2010) was employed. This paper utilized Voellmy rheology to simulate the debris flow process and validate the performance of the

95 numerical model using the theoretical experiments of Bouchut and Zeitlin (2010) and Krvavica (2020), and laboratory experiment of Rzedkiewicz et al. (1997). Additionally, to examine the model's applicability at a field scale, sensitivity analysis was performed by considering the reservoir collapse event caused by landslide–debris flows in Sanyang Reservoir, Icheon, South Korea, in 2020. This study precisely simulated the flow processes to consider essential factors in debris flow, such as



erosion, entrainment, and deposition processes (Lee et al., 2022a; b). The sensitivity analysis was conducted by constructing scenarios that incorporated the characteristics of debris flow, such as its density and rheology parameters, as well as the water level of the reservoir.

2 Materials and methods

2.1 Numerical modeling

2.1.1 Governing equation

Recently, analysis methods using two-phase or multiphase techniques have been vigorously studied to simulate and analyze debris flow dynamics precisely (Pudasaini and Mergili, 2019; Mergili et al., 2020; Shugar et al., 2021). However, further research into the multilayer approach, which explores complex dynamics between distinct systems, such as the interaction between debris flow and water when debris flow enters a water system, is necessary. Studies on multilayer fluid dynamics have included several research efforts to enhance stability and accuracy through mathematical theories (Bouchut and Zeitlin, 2010; Benkhaldoun et al., 2014). However, a practical utilization of the multilayer approach in debris flow analysis is scarce. Therefore, the model developed in this study simulated the debris flow and water using one-dimensional shallow water equations based on the Navier–Stokes equations. Shallow water equations are commonly used to interpret natural fluid phenomena, such as floods and debris flows, where horizontal flow dominates over vertical flow. The phenomenon under investigation in this study also exhibits dominant horizontal flow compared to vertical flow. Therefore, shallow water equations were employed to efficiently simulate this field-scale phenomenon. The hyperbolic conservation form of the mass and momentum balance equation for the debris flow layer is expressed as follows:

$$\begin{cases} \partial_t h_j + \partial_x(h_j u_j) = \begin{cases} Q & \text{if } j = \text{debris flow} \\ 0 & \text{else if } j = \text{water} \end{cases} \\ \partial_t(h_j u_j) + \partial_x(h_j u_j^2 + g h_j^2 / 2) + g h_j \partial_x \left(z + \sum_{k>j} h_k + \sum_{k<j} \frac{\rho_k}{\rho_j} h_k \right) = S_g - S_f \end{cases}, \quad (1)$$

where t denotes time, x is the Cartesian coordinates, j is the number of layers, h is the depth of the fluid, u represents the depth-averaged velocity components in the x direction at each layer, g is the acceleration of gravity, ρ_j is the mass density of the layer j , Q is the term for simulating the erosion-entrainment ($Q>0$) and deposition processes ($Q<0$), S_g represents the gravitational acceleration in the x direction, and S_f represents the driving friction in the x direction. The water layer equations are almost the same as those of the debris flow layer. Because the water layer does not have a source term for the mass balance equation, the system has no sink/source. Each layer should be located at the bottom in order of density (Bouchut and Zeitlin, 2010). For example, when analyzing debris flow and water through a bilayer, the debris flows with a relatively high density must be located at a lower position than the water. This study considers the friction between debris flow and water, and S_f , which reflects this, is calculated as follows:



$$S_f = \begin{cases} S_{debris} + S_{interface} & \text{if } j = \text{debris flow} \\ S_{interface} + S_{manning} & \text{else if } j = \text{water} \end{cases}, \quad (2)$$

where S_{debris} is shear stress for considering the debris flow behaviour; $S_{interface}$ is friction between two contact layers; and $S_{manning}$ is the Manning friction to simulate the momentum transfer process in water propagation, designed to activate only when the debris flow is in dry conditions ($h_{debris}=0$). Thus, in grid cells where water and debris coexist, both S_{debris} and $S_{interface}$ are applied to the debris flow, while only $S_{interface}$ is applied to the water. In grid cells containing only debris flow, only S_{debris} is applied, and in cells with only water, $S_{manning}$ is applied. The shear stress of debris flow is given by the Voellmy rheology as follows (Voellmy, 1955):

$$S_{debris} = \mu g h_j + \frac{g u_j^2}{\xi}, \quad (3)$$

where μ and ξ , the Coulomb friction and turbulent friction coefficients, dominate the deceleration behavior when the flow is slow and fast, respectively (Bartelt et al., 2013; Frank et al., 2015). In this study, the mechanism proposed by Canestrelli et al. (2012) was utilized to consider the friction force occurring between debris flow layer and water layer. The mechanism of $S_{interface}$ is as follows:

$$S_{interface} = \frac{\rho_0 f^{int}}{\rho_k} \Delta u u, \quad (4)$$

where ρ_0 is the mass density of the water; $\Delta u = U_1 - U_2$, while U_k denotes the flow depth (h_k) or the momentum ($h_k u_k$) of the fluid in each layer, and f^{int} is the interface friction coefficient. The mechanism of Manning friction $S_{manning}$ is as follows:

$$S_{manning} = \frac{g n^2 u^2}{h_{water}^{1/3}}, \quad (5)$$

where n is the Manning's roughness coefficient. This study set Manning's roughness coefficient n as 0.01 based on Arcement and Schneider (1989). Moreover, the algorithm for three debris flow processes (Q : erosion, entrainment, deposition rate) proposed by Lee et al. (2022b) is as follows:

$$Q(x, t) = \begin{cases} dz/dt_e & \text{if } \tau = \rho g h s > \tau_e \\ dz/dt_d & \text{else if } \tau < \tau_d \\ 0 & \text{else} \end{cases}, \quad (6)$$

$$h_{max}(x, 0) = \begin{cases} dz/d\tau (\tau - \tau_e) & \text{if } \tau > \tau_e \\ 0 & \text{else} \end{cases}, \quad (7)$$



where dz/dt_e is the constant erosion-entrainment rate; dz/dt_d is the constant deposition rate; $h_{max}(x,0)$ is the maximum potential erosion depth; τ is the shear stress of the layer (j); τ_e and τ_d are the critical shear stress of erosion and deposition, respectively; $dz/d\tau$ is the average potential erosion depth; and s is the channel slope. Notably, this mechanism only affects the debris flow layer not the water layer.

2.1.2 Spatial and temporal discretization

The governing equation was discretized using FVM. Numerical models that utilize shallow-water governing equations often suffer from an imbalance between the gradient of the water depth and bed slope in irregular topography. This imbalance may cause nonphysical perturbations and instability of the simulation near shocks or wet-dry transitions. Numerous well-balanced numerical schemes have been proposed (e.g. Audusse et al., 2004; Audusse and Bristeau, 2005; Caleffi et al., 2006; Kim et al., 2008; Caleffi and Valiani, 2009). This model implements the hydrostatic reconstruction technique proposed by Audusse et al. (2004), which has been successfully applied to shallow-water models. For stable multilayer simulation and analysis based on shallow water equations, the UDCHR scheme proposed by Bouchut and Zeitlin (2010) was applied. The discretized governing equation for each layer is written as follows:

$$\frac{A_i}{\Delta t}(\mathbf{q}_i^{n+1} - \mathbf{q}_i^n) + \mathbf{F}_i = \mathbf{S}_i + \mathbf{S}c_i + \mathbf{S}f_i + \mathcal{J}_i, \quad (8)$$

where A_i is the area of the cell (i); \mathbf{q} refers to the state variables such as flow depth and momentum at cell i for the n -th time step; $\mathbf{S}c_i$ is an additional source term to balance the presence of a source; $\mathbf{S}f_i$ is the entrainment source term and driving friction term; \mathcal{J}_i is an additionally introduced term for the numerical stability of multilayer shallow water system; and \mathbf{F}_i is the numerical flux term, which is defined as

$$\mathbf{F}_i = l_{i,r}\mathbf{F}_{i+1/2} - l_{i,l}\mathbf{F}_{i-1/2}, \quad (9)$$

where $l_{i,p}$ is the length of the cell face p in cell (i) and the subscripts $p=\{r,l\}$ indicate that the respective value is constructed on the right or left side of the cell, respectively. Notably, the (i) index is used on a uniform template and $i\pm 1/2$ indicates the cell face on the uniform grid to clearly describe the numerical scheme in a one-dimensional space. Each flux term is calculated as follows:

$$\mathbf{F}_{i+1/2} = \mathcal{F}(\mathbf{q}_{i+1/2-}, \mathbf{q}_{i-1/2+}), \quad \mathbf{F}_{i-1/2} = \mathcal{F}(\mathbf{q}_{i-1/2-}, \mathbf{q}_{i-1/2+}), \quad (10)$$

where \mathcal{F} is the numerical flux solver. The interface conserved values are defined as

$$\mathbf{q}_{i+1/2-} = \begin{pmatrix} h_{i+1/2-} \\ h_{i+1/2-}u_{i,r} \end{pmatrix}, \quad \mathbf{q}_{i-1/2+} = \begin{pmatrix} h_{i+1/2+} \\ h_{i+1/2+}u_{i,l} \end{pmatrix}, \quad (11)$$



with the following hydrostatic reconstruction:

$$175 \quad h_{i+1/2-} = \max(0, h_{i,r} + z_{i,r} - z_{i+1/2}), \quad h_{i+1/2+} = \max(0, h_{i+1,l} + z_{i+1,l} - z_{i+1/2}), \quad (12)$$

where $u_{i,p}$, $h_{i,p}$, and $z_{i,p}$ are the reconstructed values for the second-order accuracy at the cell interface p of cell (i) and $z_{i+1/2} = \max(z_{j,i,r}, z_{j,i+1,l})$. $z_{j,i}$ is defined as

$$z_{j,i} = z_i + \sum_{k>j} h_{k,i} + \sum_{k>j} \frac{\rho_k}{\rho_j} h_{k,i}, \quad (13)$$

The source terms are defined as

$$180 \quad \mathbf{S}_i = l_{i,r} \mathbf{S}_{i+1/2} - l_{i,l} \mathbf{S}_{i-1/2}, \quad (14)$$

$$\mathbf{S}_{i+1/2} = \begin{pmatrix} 0 \\ gh_{j,i+1/2-}^2/2 - gh_{j,i,r}^2/2 \end{pmatrix}, \quad \mathbf{S}_{i-1/2} = \begin{pmatrix} 0 \\ gh_{j,i-1/2+}^2/2 - gh_{j,i,l}^2/2 \end{pmatrix}.$$

Additional source terms to ensure balance for the second order scheme are defined as

$$\mathbf{Sc}_i = -l_{i,r} \mathbf{Sc}_{i,r} + l_{i,l} \mathbf{Sc}_{i,l}, \quad (15)$$

$$\mathbf{Sc}_{i,r} = \begin{pmatrix} 0 \\ g(h_{j,i,r} + h_{j,i})(z_{j,i,r} - z_{j,i})/2 \end{pmatrix}, \quad \mathbf{Sc}_{i,l} = \begin{pmatrix} 0 \\ g(h_{j,i,l} + h_{j,i})(z_{j,i,l} - z_{j,i})/2 \end{pmatrix}.$$

\mathcal{J} is computed as follows (Bouchut and Zeitlin, 2010):

$$\mathcal{J} = \begin{pmatrix} \mathcal{J}^0 \\ \mathcal{J}_p^1 \end{pmatrix}, \quad (16)$$

185 where \mathcal{J}^0 is a term affecting the continuity equation and \mathcal{J}_p^1 affects the momentum equation. \mathcal{J}^0 is defined as

$$\mathcal{J}^0 = \frac{1}{2}((1 + \theta)u_l + (1 - \theta)u_r)\kappa, \quad (17)$$

where θ and κ are calculated as follows:

$$\theta = \min\left(1, \frac{(u_l)_+}{\sqrt{gh_l}}\right) - \min\left(1, \frac{(-u_r)_+}{\sqrt{gh_r}}\right), \quad (18)$$

$$\kappa = \begin{cases} \tilde{\kappa} & \text{if } |\tilde{\kappa}| \leq \frac{5}{2} \min(h_l, h_r) \\ \frac{5}{2} \min(h_l, h_r) & \text{else} \end{cases}, \quad (19)$$



190 where $(u_p)_+ = \max(0, u_p)$ and $(u_p)_- = \min(0, u_p)$; $\tilde{\kappa}$ and $\hat{\kappa}$ in Eq. (19) is defined as

$$\tilde{\kappa} = \hat{\kappa} + \left((\underline{\Delta z})_+ - \hat{\kappa} \right) \min \left(1, \frac{1}{4} \frac{(u_l)_+}{\sqrt{gh_l}} \right) + \left((-\underline{\Delta z})_+ - \hat{\kappa} \right) \min \left(1, \frac{1}{4} \frac{(-u_r)_+}{\sqrt{gh_r}} \right), \quad (20)$$

$$\hat{\kappa} = \frac{1}{2} |\underline{\Delta z}| + \begin{cases} \frac{1}{2} \frac{(\Delta z - h_l)h_r}{h_r + \Delta z - h_l} & \text{if } \Delta z > h_l \\ \frac{1}{2} \frac{-(h_r + \Delta z)h_l}{h_l - (h_r + \Delta z)} & \text{else if } \Delta z < -h_r \\ 0 & \text{else} \end{cases}, \quad (21)$$

where $\underline{\Delta z} = \min(\Delta z, h_l)$ when $\Delta z \geq 0$ and $\underline{\Delta z} = \max(\Delta z, -h_r)$ when $\Delta z \leq 0$ and Δz is the difference between the contacted cells, calculated as $z_{i,r} - z_{i+1,l}$. \mathcal{J}_p^1 in Eq. (16) is defined as

$$195 \quad \mathcal{J}_l^1 = \delta_l + \mathcal{J}^1, \quad \mathcal{J}_r^1 = -\delta_r + \mathcal{J}^1, \quad (22)$$

where \mathcal{J}^1 is calculated as $\mathcal{J}^1 = u_l(\mathcal{J}^0)_+ + u_r(\mathcal{J}^0)_-$ and δ_p is defined as

$$\begin{aligned} \delta_l &= \frac{1}{2} (1 + \theta) g (h_r - h_l + \Delta z) \kappa, \\ \delta_r &= \frac{1}{2} (1 - \theta) g (h_r - h_l + \Delta z) \kappa. \end{aligned} \quad (23)$$

The numerical fluxes in Eq. (8) are calculated using the Harten–Lax–van Leer contact approximate Riemann solver in the developed model. Therefore, the conservative values over the time step Δt are calculated as follows:

$$200 \quad A_i \mathbf{q}_i^{n+1} = A_i \mathbf{q}_i^n - \Delta t (\mathbf{F}_i - \mathbf{S}_i - \mathbf{S} \mathbf{c}_i - \mathbf{S} \mathbf{f}_i - \mathcal{J}_i), \quad (24)$$

The additional source/sink terms for entrainment and driving friction force are written as

$$\mathbf{S} \mathbf{f}_i = \begin{pmatrix} Q \\ S_f \end{pmatrix}. \quad (25)$$

The inclusion of a friction term can cause numerical instability within a discretized domain, particularly when a dry–wet transition exists (An et al., 2019). In other words, if the flow depth approaches zero, driving friction can result in an exaggerated
205 force, which reverses the flow in a non-physical manner. Therefore, the friction term should be properly treated. The developed model implements an implicit discretization based on the splitting method (Liang and Marche, 2009), which is equivalent to solving the following equation:

$$\frac{d\mathbf{q}_i}{dt} = \mathbf{S} \mathbf{f}_i. \quad (26)$$



The Euler implicit discretization of the above equation yields the following:

$$210 \quad \frac{\mathbf{q}_i^{n+1} - \mathbf{q}_i^n}{\Delta t} = \mathbf{Sf}_i^{n+1}. \quad (27)$$

The right side of Eq. (27) can be represented by the Taylor series expansion as

$$\mathbf{Sf}_i^{n+1} = \mathbf{Sf}_i^n + \left(\frac{\partial \mathbf{Sf}}{\partial \mathbf{q}} \right)_i^n (\Delta \mathbf{q}_i) + o(\Delta \mathbf{q}_i^2), \quad (28)$$

where $\Delta \mathbf{q} = \mathbf{q}_i^{n+1} - \mathbf{q}_i^n$. Ignoring high-order terms and substituting Eq. (27) into Eq. (26) yields

$$\mathbf{q}_i^{n+1} = \mathbf{q}_i^n + \Delta t \cdot \mathbf{D}^{-1}(\Delta t) \cdot \mathbf{Sf}_i^n, \quad (29)$$

215 where

$$\mathbf{D}(\Delta t) = \left(\mathbf{I} - \Delta t \left(\frac{\partial \mathbf{Sf}}{\partial \mathbf{q}} \right)_i^n \right), \quad (30)$$

where \mathbf{I} is a unit matrix and

$$\frac{\partial \mathbf{Sf}}{\partial \mathbf{q}} = \begin{pmatrix} \frac{\partial Q}{\partial h} & \mathbf{0} \\ \mathbf{0} & \frac{\partial S_f}{\partial (hu)} \end{pmatrix}, \quad (31)$$

Equation (29) ignores the effects of off-diagonal entries. This method can be successfully applied to shallow water systems

220 with Manning friction (An and Yu, 2014). Denoting $\bar{\mathbf{Sf}}_i^n(\Delta t) = \mathbf{D}^{-1}(\Delta t) \cdot \mathbf{Sf}_i^n$ yields the implicit scheme written as

$$\begin{aligned} A_i \mathbf{q}_i^{n+1*} &= A_i \mathbf{q}_i^n - \Delta t (\mathbf{F}_i^n - \mathbf{S}_i^n - \mathbf{Sc}_i^n - \mathcal{J}_i^n), \\ \mathbf{q}_i^{n+1} &= \mathbf{q}_i^{n+1*} + \Delta t \cdot \bar{\mathbf{Sf}}_i^n(\Delta t). \end{aligned} \quad (32)$$

Although the friction terms are implicitly discretized, the friction force in Eq. (31) can cause exaggerated reverse flow, which is physically implausible (An et al., 2019). Therefore, if the driving friction results in reverse flow, the fluid flow stops. The time step Δt is determined in each step based on convergence by the Courant–Friedrichs–Lewy condition as follows:

$$225 \quad \Delta t = C \min_{j,i} \left(\frac{\Delta x}{\alpha_{SCHR}} \right) = C \min_{j,i} \left(\frac{\Delta x}{\alpha^{\mathcal{F}} + \alpha^{\mathcal{J}}} \right), \quad (33)$$

$$\alpha^{\mathcal{F}} = |u_{j,i}| + \sqrt{gh_{j,i}}, \quad (34)$$



$$\alpha^{\mathcal{J}} = 2 \left(\frac{(\mathcal{J}^0)_+}{h_l} + \frac{(-\mathcal{J}^0)_+}{h_r} \right), \quad (35)$$

where C , a dimensionless number called the Courant number, was set as 0.5 in this study. This study utilized the experimental results of Bouchut and Zeitlin (2010), Krvavica (2020), and Rzadkiewicz et al. (1997) to validate the model performance. The validation is described in the following subsection.

2.2 Validations

In this section, the model developed in this study is validated. First, this study conducted fundamental numerical validations based on three theoretical experiments of Bouchut and Zeitlin (2010) and Krvavica (2020). Moreover, to validate the performance in real situations the numerical model developed in this study is validated in the submarine landslides and wave generation against the experimental tests of Rzadkiewicz et al. (1997).

2.2.1 Theoretical experiments

It is essential not only to perform tests in experiments and field events but also to test numerical performance at the mathematical and programming levels to utilize the developed numerical model. This study used the three validation cases in Bouchut and Zeitlin (2010) and Krvavica (2020).

The validation results in Fig. 1 show that light blue represents the upper layer, dark blue depicts the lower layer, and the black solid line signifies the analytical solution for the lower or upper layer. Figure 1a is a case in Bouchut and Zeitlin (2010), where the density of the upper layer is 0.95 times that of the lower layer, with the simulation at 0.5 s later depicted in Fig. 1d. Figure 1b, Test II: an internal collision of two dam breaks from Krvavica (2020), shows a condition where the density of the upper layer is 0.98 times that of the lower layer, with the state 25 s later shown in Fig. 1e. Figure 1c corresponds to Test IV: an internal dam break from Krvavica (2020), where the upper layer's density is 0.4 times that of the lower layer, and the simulation 5 s later is shown in Fig. 1f. As demonstrated in Fig 1, the performance of numerical model developed in this study has been confirmed to be well-constructed both mathematically and programmatically.

2.2.2 Laboratory experiment: subaqueous debris flow

Rzadkiewicz et al. (1997) experimented with the subaqueous soil slope failure scenario, as shown in Fig. 2a, and they set a debris density of 1,950 kg/m³ and a water density of 1,000 kg/m³. Rzadkiewicz et al. (1997) presented experimental results on water surface and debris flow behavior at 0.4 s and 0.8 s, as depicted in Fig. 3, respectively.

Figure 3a reveals the reproducibility of water levels, where the plotted dots represent the observed values from Rzadkiewicz et al. (1997), and the solid red line indicates the simulation results from this study. Figure 3b presents the overall simulation results, focusing on the reproducibility of debris flow. In this figure, the blue solid line represents water levels, the red solid line represents debris flow, the black solid line represents topography, and the red dotted line corresponds to the debris flow



thickness observed in Rzadkiewicz et al. (1997). In this study, to simulate the experiment of Rzadkiewicz et al. (1997), the parameters of Voellmy rheology and the interface friction coefficient were calibrated to $\mu=0.15$, $\zeta=50$ m/s², and $f^{int}=10.0$, respectively. The three parameters were calibrated through back-analysis, but their values were set within the range presented and suggested in previous studies. In this context, the value of ζ is significantly lower than those used in previous studies (e.g. Cesca and D'Agostino, 2008; Frank et al., 2015), while f^{int} is notably higher (Canestrelli et al., 2012). It has been attributed to the reduced fluidity and increased resistance from water, as the analysis pertains not to a typical debris flow but to slopes that collapsed underwater. However, since these values do not deviate substantially from the range used in prior research, they have been assessed as reasonable.

At 0.4 s, the simulation results aligned well with the experimental observations, accurately capturing the water level reduction around 1.5 m. At 0.8 s, the simulation also exhibited good agreement with the experimental data, particularly in reproducing the water level patterns. However, the simulation failed to capture the fine oscillations of the water level. This phenomenon is believed to occur due to the abrupt collapse of sediment along the slope. In areas where the sediment layer becomes thinner (around 1.0–1.5 m), negative pressure is exerted on the water, whereas in areas where the sediment layer thickens (around 1.5–2.0 m), positive pressure is exerted. A hydraulic jump-like appears at the intersection of these negative and positive pressures, near 1.5 m—where the water layer thickens rapidly—drawing water toward the negative pressure region. It has been identified that the numerical model developed in this study has limitations in accurately simulating this phenomenon. Nevertheless, comparing the simulated results with experimental observations reveals that while the reproduction of microscopic details was somewhat limited due to the depth-average shallow water modeling characteristics, the model demonstrated satisfactory accuracy in macroscopic aspects such as wave height and propagation velocity. R^2 and RMSE (Root Mean Square Error) analysis was conducted to validate the accuracy of the simulation results. The R^2 for the water surface oscillation and debris flow thickness were 0.876 and 0.823, respectively. The RMSE values for these results were 0.016 m and 0.060 m, respectively, indicating low discrepancies between the simulation results and experimental observations. The model developed in this study successfully simulated three theoretical experiments and the laboratory experiment. This study analyzed the wave caused by landslide–debris flows occurring in the field scale based on a hypothetical method using our model. The following section discusses this in detail.

3 Field-scale analysis

3.1 Study area and event

This study conducted a two-layer dynamic flow analysis for Sanyang Reservoir in Icheon, Gyeonggi, South Korea. The Korea Rural Community Corporation (KRC) designed and constructed it in 1966, and it is managed by Icheon City. According to the KRC, the reservoir is a small-scale agricultural reservoir with a fill dam 9.5 m high and 126 m long. It has been in operation for over 50 years, making it an aging reservoir (Fig. 4). Sanyang Reservoir has a catchment area of 192 ha, a surface area of



2.8 ha, and an effective storage capacity of 60,000 tons and serves as a water storage facility for agricultural purposes (<https://rawris.ekr.or.kr/main.do>).

Despite receiving a “satisfactory” safety rating in the first half of 2020 from the KRC’s reservoir safety assessment, the
290 Sanyang Reservoir collapsed due to concentrated heavy rainfall of 193 mm/7 h on 2 August, 2020, between 00:00 and 07:00. The collapse reportedly occurred at 07:30. Although no casualties were reported, approximately 10 houses were flooded, and 6 ha of fields and rice paddies were inundated, resulting in significant property damage (Fig. 4).

The explicit cause of the dam collapse has not been investigated and reported. However, aerial photographs before and after the incident, as shown in Fig. 5, yield evidence of landslides and debris flows. Figures 8a and 8b show satellite images taken
295 at the same locations as those in Figs. 4a and 4b, respectively, before and after the incident. According to news and media, numerous landslides and debris flow events occurred in Ichon City during the same period. Therefore, this study assumed that external rather than internal factors were behind the reservoir collapse. In this context, the external factors are assumed to be landslides and debris flow, based on Fig. 4 and news reports.

This reservoir has a history of collapse, which occurred in 1970, and the recent incident marks the second collapse. Therefore,
300 this facility had a risk of future collapse. Consequently, numerical modeling is imperative for efficient operation and the development of stable countermeasures for such regions. This study utilized the developed model to simulate and analyze the phenomenon of sediment inflow in Sanyang Reservoir. However, we could not determine the reservoir water level at the time of the collapse due to inadequate field data for the incident period. Therefore, this study assumed that the reservoir water level at the time of the incident was at the flood level (119 m), considering that the incident occurred during the flood season (06.21.–
305 09.20., as established by the Ministry of Government Legislation in South Korea).

The input data used for the analysis are shown in Fig. 6. The topographic data utilized a 5 m by 5 m resolution digital elevation model (DEM) provided by the National Geographic Information Institute of South Korea (Fig. 6a). As the model in this study used is a one-dimensional analysis, it requires the establishment of flow paths for debris flow. Therefore, this study calculated the flow paths of the basin, depicted by the red solid line in Fig. 6a. The traces of debris flow observed in Figs. 4 and 5 suggest
310 that the debris flow entered the reservoir from flow path 2. Figure. 6b illustrates the cross-section of the flow path 2, and Fig. 6c depicts the topography near the reservoir.

This study assumed that the internal topography of the reservoir is linear based on the reservoir information. Reservoir water level fluctuations by debris flow were observed at points p1, p2, and p3, as marked with red arrows in Fig. 6c.

The slope of each point data point was used to estimate the location of the landslide occurrence on the slope, as shown in Fig.
315 7a. Previous research by Ma et al. (2022) indicated that locations with slopes of more than 40° have a high risk of landslide–debris flow occurrence. Therefore, the slope exceeding 40° experienced slope failure and liquefaction, resulting in debris flow (Fig. 7b). Considering the limited analysis of the structure in the numerical model used in this study, the risk of the structure was considered to increase following an overflow, in accordance with the characteristics of the fill dam.



3.2 Simulation results and discussion

320 The Sanyang Reservoir basin was simulated based on Section 3.1. Figure 8 and movie S1 show debris flow entering the reservoir and causing water level fluctuations. Table 1 summarizes the parameter values used in Fig. 8 and movie S1, which were determined based on the analysis in Section 3.1 and previous research on debris flow cases in South Korea (e.g. An et al. 2019; Lee et al. 2022b, 2023). This study assumed that the soil depth was 1 m, and the location of the debris flow initiation was determined based on Fig. 6, assuming that the collapse occurred to the depth of the sediment at that point. As shown in
325 movie S1, the erosion, transport, and deposition processes resulting from the friction between the sediment and the ground during the sediment and debris flow movement on the slope were considered in the numerical simulation as elevation changes. However, as infiltration and erosion processes are typically controlled within the reservoir, this study assumed that these erosion processes caused by debris flow did not occur inside the reservoir.

After the collapse of the slope, debris flow entered the reservoir after 248 s. By 300 s, most debris flows had stopped and
330 started depositing within the reservoir (Fig. 8 and movie S1). Although no overflow occurred in this simulation, the water level in the reservoir rose significantly, threatening the stability of the structure, and continuous waves were observed even after 400 s.

It is essential to consider various conditions and conduct thorough analyses to assess such ungauged basins and predict potential future scenarios. Therefore, this study conducted a two-layer dynamic analysis with different parameter variations based on
335 the range of Voellmy parameters proposed in previous studies (Pirulli and Sorbino 2008; Hussin et al. 2012; Frank et al. 2015). This study compared and analyzed the wave characteristics observed at points p1, p2, and p3 in Fig. 6 according to the parameter settings. The numerical simulation was conducted with the same water level as the previous case (119 m), and the freeboard to the top of the dam at the flood level was approximately 0.4 m (Fig. 6).

The water level fluctuations over time at p1, p2, and p3 were analyzed by fixing ξ at 500 m/s^2 and controlling μ , as shown in
340 Fig. 9. In Voellmy rheology, μ is a parameter representing the viscosity of debris flow, where an increase in μ leads to a slower flow, as previously analyzed by Lee et al. (2020). Previous studies have proposed a range of μ from 0.01 to 0.20; however, this study adjusted it within the range of 0.03 to 0.05, referring to simulation research of debris flow events in South Korea (An et al. 2019; Lee et al. 2022a, b, 2023, 2024). As observed in Fig. 9, even with a fine-tuned μ value of 0.005, the wave amplitude caused by the inflow of debris flow varied by approximately 0.3 m as the μ value decreased. This variation highlights
345 the sensitivity of wave dynamics to the μ value. As μ increased, the mobility of the debris flow decreased, resulting in a reduction in wave amplitude, illustrating the influence of μ on both debris flow mobility and the resulting wave characteristics. Particularly for p1, despite a freeboard of 0.4 m to the top of the dam, the water level increased to 1.25 m. This phenomenon occurred because the debris flow was deposited higher than the water level, resulting in an elevation change. In other words, when μ is lower than 0.05, the elevation at p1 can rise to 1.25 m, which directly damages the effective reservoir capacity. These
350 findings suggest that variations in μ can significantly impact water levels. A μ value lower than 0.05 can deteriorate reservoir function due to the debris flow deposition in the reservoir.



At p2 and p3, the water level, as analyzed, rises to 0.5 m when μ is lower than 0.05, causing an overflow. Consequently, for Sanyang Reservoir, a structure comprising a fill dam, the presence of highly mobile debris flow with μ lower than 0.05 poses a significant risk of generating waves and potential structure collapse. Among the observed points, p3, closest to the structure, exhibited the highest wave amplitude. This phenomenon is assessed based on the superposition of reflected waves from the structure, and it can cause a significant impact not only on fill dams but also on concrete dams. However, as observed in Fig. 9, the magnitude of the waves decreased rapidly over time at p1, p2, and p3. The water level of the reservoir stabilized 500 s after the debris flow release.

When μ was fixed at 0.05, and ζ was adjusted, the water level variations over time at p1, p2, and p3 were analyzed as shown in Fig. 10. According to Lee et al. (2020), in Voellmy rheology, ζ is the turbulent friction coefficient, and lower values are associated with a decrease in debris flow velocity. Previous studies proposed a range of ζ from 15 m/s² to 2000 m/s², but this study controlled ζ from 400 m/s² to 1500 m/s², referring to simulation research of debris flow events in South Korea (An et al. 2019; Lee et al. 2022a, b, 2023, 2024). Although ζ decreased, leading to a decline in the mobility of the debris flow, the significant variation in ζ within the applied range, as shown in Fig. 10, did not result in as notable a change in wave height compared to the sensitivity observed with μ . The water level at p1 in Fig. 9 was attributed to topographical changes due to debris flow deposition. However, in Fig. 10, it was analyzed that the continuous wave was transmitted at p1 because the height of the deposited debris flow did not exceed the water level. When ζ was set to 1500 m/s², the second wave at p1 showed an increase of approximately 0.2 m in wave height compared to the first wave, indicating that the magnitude difference between the first and second waves was amplified depending on the parameter setting. However, regardless of the parameter setting, the second wave at all points (p1, p2, and p3) was more significant in magnitude than the first wave.

According to Fig. 10, even 600 s after the debris flow was released, the water level continues to fluctuate steadily at p1 and p3 due to the waves. However, at p2, the water level stabilized after 400 s because the waves reflected from the structure overlapped with the waves generated by the debris flow entering, and a wave-breaking zone was formed near p2, leading to the water level being the most stable at this point. Thus, Figs. 9 and 10 show distinct simulation results because in Fig. 9, overflow occurred in most cases, causing the energy of the waves to dissipate sufficiently. Therefore, waves with low energy were reflected from the structure, and they had less wave superposition. However, in Fig. 9, overflow hardly occurred, and the energy of the waves was conserved within the reservoir. Consequently, at p1 and p3 in Fig. 10, the waves persisted for a long time.

The analysis of the waves shown in Figs. 9 and 10 and the simulation results of debris flow for each scenario are summarized in Table 2. Additionally, this study has extensively analyzed the situations that may occur due to debris flow into Sanyang Reservoir, not only for the flood level scenario at an elevation of 119 m but also for the high-water level scenario at an elevation of 118 m, as listed in Table S1. As indicated in Tables 2 and S1, as the value of μ decreases, the height and velocity of debris flow increase, leading to an increase in the momentum of the debris flow. Conversely, as ζ decreases, the debris flow height, velocity, and momentum increase.



385 Furthermore, after the debris flows into the reservoir, the horizontal flow distance of the debris flow and the amplitude of the first wave caused by the debris flow exhibited an increasing trend with higher debris flow height, velocity, and momentum. Several studies have quantitatively analyzed the dynamic characteristics of debris flow and its interaction with waves (Fritz et al. 2004; Heller and Hager Willi 2010; Mulligan and Take 2017; Bullard et al. 2019; de Lange et al. 2020). However, they were conducted in laboratory-scale artificial slopes, which limits their direct application to natural slopes. Therefore, this study
390 quantitatively analyzed the relationship between debris flow and waves at the field scale, and the results are presented in Fig. 11 and Table 3.

Figure 11 and Table 3 are the analysis results based on Table S1, which comprehensively considers the rainy season (high-water level and flood-level scenarios). Figures 11a, b, and c depict the maximum debris flow height near the reservoir and its relationships with (a) the underwater flow distance of debris flow after inflow into the reservoir, (b) the amplitude of the first
395 wave, and (c) the maximum crest amplitude. Similarly, Figs. 11d, e, and f demonstrate the maximum velocity of debris flow near the reservoir and its relationships with (d) the underwater flow distance, (e) the amplitude of the first wave, and (f) the maximum crest amplitude. Figures 11g, h, and i show the maximum momentum near the reservoir and its relationships with (g) the underwater flow distance, (h) the amplitude of the first wave, and (i) the maximum crest amplitude. As shown in Fig. 11, the maximum debris flow height and velocity have a few correlations with the abovementioned factors. However, the
400 debris flow momentum exhibited high correlations with the abovementioned factors. Table 3 summarizes the quantified results of these relationships.

As observed in Fig. 11, the three factors (Underwater flow distance, Amplitude of the first wave, and Maximum crest amplitude) can be derived from the maximum debris flow height by multiplying it by 21.704, 0.142, and 0.203, respectively. These calculated R^2 values were satisfactory (0.862, 0.837, and 0.802), indicating their ability to predict the underwater flow distance
405 well but relatively poor ability at predicting the wave characteristics. The maximum velocity corresponded to R^2 values of 0.842, 0.787, and 0.790 for each factor, which is lower than the maximum flow height for all factors. The maximum momentum exhibited high R^2 values of 0.964, 0.985, and 0.983 for each factor, indicating its solid predictive capability for underwater flow distance and wave properties compared to the debris flow height or velocity.

Based on the correlations derived from Table 3, the debris flow data were used to predict the three abovementioned factors.
410 This study analyzed their accuracy for the high-water and flood-level scenarios, as listed in Table 4, where the accuracy of the regression equation derived in Table 3 was quantitatively evaluated using the R^2 and the RMSE. The flood level scenario could be predicted more accurately than the high-water level scenario. However, R^2 decreased significantly in the high-water level scenario for the maximum debris flow velocity, indicating limited usability. In contrast, the maximum momentum exhibited the most stable accuracy for all metrics, regardless of the water level in the reservoir. Therefore, momentum data are considered
415 adequate for analyzing the characteristics of the waves generated when debris flows into the reservoir, similar to those in Table 3.

The water level change due to debris inflow according to differences in water-level scenarios is depicted in Fig. 12, and the parameter settings used in this analysis are the same as those listed in Table 1. According to Fig. 12, when debris flows into



the reservoir, the water level generally increases by 1.3–1.5 m. In the case of the flood level, this indicates the occurrence of an overflow. Moreover, when the water level at the debris flow occurrence lies between the high-water and flood levels, overflow may occur. In the case of Sanyang Reservoir, which saves water through a fill dam, the possibility of dam collapse significantly increases when an overflow occurs. Specifically, reservoirs with small storage, such as Sanyang Reservoir, are expected to experience significant water level fluctuations due to debris flow entering. Therefore, systematic water level control during flood periods is essential in the small reservoirs constructed as fill dams.

4 Limitation and further study

Although this paper did not present results on parameter settings that μ was higher than 0.05 or ζ was lower than 200 m/s², in these cases, the debris flow did not reach the reservoir and, thus, did not inflow into it. Determining the characteristics of the generated debris flow would be helpful to parties interested in assessing the occurrence of complex hazards and understanding the magnitude of waves caused by landslide–debris flow, based on Tables 2 and 3 and Figs. 9 and 10. However, real-time measurements of the properties of debris flow are almost impossible, and even if these can be known, the Voellmy rheology used in this study contains conceptual methodology, limiting the applicability of field data. Therefore, scenario-based analyses are essential.

Nevertheless, the one-dimensional models have limited capability in two- and three-dimensional interpretation. Hence, additional research must be conducted by expanding to at least two-dimensional models to analyze complex hazards precisely.

Moreover, further analysis techniques for evaluating the stability of structures against waves should be developed. Therefore, in future studies, additional research that considers the impact of waves in two- or three-dimensional-based numerical models for areas where structures collapse or secondary flood damage occurs due to overflow should be performed.

5 Conclusion

Landslide–debris flow occurring in basins with dams or reservoirs can not only deteriorate the function of facilities but also potentially cause tsunami-type waves due to the rapid influx of a large amount of sediment (complex hazards). Numerical modeling analysis is essential to prevent and effectively respond to such complex hazards. Some researchers have used the SPH method to analyze complex hazards; however, this technique has the limitation of requiring long simulation times, making it less efficient for various cases. Therefore, this study developed a one-dimensional numerical model based on shallow water equations with a multilayer system, which allows for the efficient analysis of complex hazards. The model was discretized using the FVM and used Voellmy rheology to simulate the debris flow. Moreover, this model facilitates the simulation of erosion, entrainment, and deposition processes during debris flow.

This study cited theoretical experiment results (Bouchut and Zeitlin, 2010; Krvavica, 2020) and laboratory-scale experiment results conducted on artificial slopes (Rzadkiewicz et al., 1997) to evaluate the performance of the developed model, and the



model successfully simulated both experiments. Scenario-based analysis was performed based on the validation results for the
450 2020 Sanyang Reservoir collapse event at Icheon in South Korea.

The simulation results revealed that the wave generated by debris flow can vary significantly depending on the characteristics
of the debris flow. It was analyzed that the scale of the wave generated can be estimated based on the maximum flow height
and velocity of the debris flows. However, the accuracy of the prediction varied significantly depending on the reservoir water
level when estimating the wave scale based on the maximum flow height and velocity. However, utilizing the maximum
455 momentum of the debris flow provided a more stable and accurate estimation of the wave scale than the method based on the
maximum flow height and velocity.

Furthermore, small-scale reservoirs were found more vulnerable to complex hazards. Considering the increasing frequency
and scale of natural disasters, including landslide–debris flow and floods, on a global scale due to extreme climate events, we
expected that this study could contribute to establishing an effective and stable management system for reservoirs and dams
460 in response to natural disasters.

Data availability

Data supporting the research are obtainable from the corresponding author upon reasonable request.

Supplement

465 Author contributions

SL: Conceptualization, methodology, investigation, software, validation, visualization, writing – original draft preparation.
HA: Conceptualization, methodology, software, supervision, writing–reviewing & editing. TK: Methodology, validation. MK:
Investigation (field survey), resources (provision of data).

Competing interests

470 The authors declare that they have no conflict of interest.



Disclaimer

Publisher's note: Copernicus Publications remains neutral with regard to jurisdictional claims made in the text, published maps, institutional affiliations, or any other geographical representation in this paper. While Copernicus Publications makes every effort to include appropriate place names, the final responsibility lies with the authors.

475 Acknowledgements

This work was supported by the Korea Institute of Geoscience and Mineral Resources (KIGAM) and the Ministry of Science and ICT (South Korea MSIT).

Financial support

480 This work was supported by the Basic Research Project of the KIGAM (Project code: 25-3412) and the National Research Foundation of Korea grant funded by the South Korea MSIT (No. 2021R1A2C200553012).

Declaration of generative AI and AI-assisted technologies in the writing process

During the preparation of this work, the authors used ChatGPT in order to enhance grammatical accuracy and clarity. After using this tool/service, the authors reviewed and edited the content as needed and take full responsibility for the content of the publication.

485 References

- Abadie, S., Morichon, D., Grilli, S., and Glockner, S.: Numerical simulation of waves generated by landslides using a multiple-fluid Navier–Stokes model, *Coast. Eng.*, 57, 779–794, [doi:10.1016/j.coastaleng.2010.03.003](https://doi.org/10.1016/j.coastaleng.2010.03.003), 2010.
- Arcement, G. J. and Schneider, V. R.: Guide for selecting Manning's roughness coefficients for natural channels and flood plains, Report 2339, [doi:10.3133/wsp2339](https://doi.org/10.3133/wsp2339), 1989.
- 490 An, H. and Yu, S.: Finite volume integrated surface-subsurface flow modeling on nonorthogonal grids, *Water Resour. Res.*, 50, 2312–2328, [doi:10.1002/2013WR013828](https://doi.org/10.1002/2013WR013828), 2014.
- An, H., Kim, M., Lee, G., Kim, Y., and Lim, H.: Estimation of the area of sediment deposition by debris flow using a physical-based modeling approach, *Quat. Int.*, 503, 59–69, [doi:10.1016/j.quaint.2018.09.049](https://doi.org/10.1016/j.quaint.2018.09.049), 2019.
- Audusse, E. and Bristeau, M.-O.: A well-balanced positivity preserving “second-order” scheme for shallow water flows on unstructured meshes, *J. Comput. Phys.*, 206, 311–333, [doi:10.1016/j.jcp.2004.12.016](https://doi.org/10.1016/j.jcp.2004.12.016), 2005.
- 495 Audusse, E., Bouchut, F., Bristeau, M.-O., Klein, R., and Perthame, B. t.: A Fast and Stable Well-Balanced Scheme with Hydrostatic Reconstruction for Shallow Water Flows, *SIAM J. Sci. Comput.*, 25, 2050–2065, [doi:10.1137/s1064827503431090](https://doi.org/10.1137/s1064827503431090), 2004.



- 500 Bartelt, P., Buehler, Y., Christen, M., Deubelbeiss, Y., Graf, C., and McArdell, B.: RAMMS—rapid mass movement simulation, A modeling system for debris flows in research and practice, user manual v1. 5, debris flow, manuscript update: 31 January 2013, WSL Institute for Snow and Avalanche Research SLF, available at: http://ramms.slf.ch/ramms/downloads/RAMMS_DBF_Manual.pdf (last access: 27 February 2015), 2013.
- Benkhaldoun, F., Sari, S., and Seaid, M.: A simple multi-layer finite volume solver for density-driven shallow water flows, *Math. Comput. Simul.*, 99, 170–189, [doi:10.1016/j.matcom.2013.04.016](https://doi.org/10.1016/j.matcom.2013.04.016), 2014.
- 505 Blasone, G., Cavalli, M., Marchi, L., and Cazorzi, F.: Monitoring sediment source areas in a debris-flow catchment using terrestrial laser scanning, *Catena*, 123, 23–36, [doi:10.1016/j.catena.2014.07.001](https://doi.org/10.1016/j.catena.2014.07.001), 2014.
- Bouchut, F. and Zeitlin, V.: A robust well-balanced scheme for multi-layer shallow water equations, *Discret. Contin. Dyn. Syst.-Ser. B*, 13, 739–758, [doi:10.3934/dcdsb.2010.13.739](https://doi.org/10.3934/dcdsb.2010.13.739), 2010.
- 510 Bullard, G. K., Mulligan, R. P., Carreira, A., and Take, W. A.: Experimental analysis of tsunamis generated by the impact of landslides with high mobility, *Coast. Eng.*, 152, 103538, [doi:10.1016/j.coastaleng.2019.103538](https://doi.org/10.1016/j.coastaleng.2019.103538), 2019.
- Caleffi, V. and Valiani, A.: Well-Balanced Bottom Discontinuities Treatment for High-Order Shallow Water Equations WENO Scheme, *J. Eng. Mech.*, 135, 684–696, [doi:10.1061/\(ASCE\)0733-9399\(2009\)135:7\(684\)](https://doi.org/10.1061/(ASCE)0733-9399(2009)135:7(684)), 2009.
- Caleffi, V., Valiani, A., and Bernini, A.: Fourth-order balanced source term treatment in central WENO schemes for shallow water equations, *J. Comput. Phys.*, 218, 228–245, [doi:10.1016/j.jcp.2006.02.001](https://doi.org/10.1016/j.jcp.2006.02.001), 2006.
- 515 Canestrelli, A., Fagherazzi, S., and Lanzoni, S.: A mass-conservative centered finite volume model for solving two-dimensional two-layer shallow water equations for fluid mud propagation over varying topography and dry areas, *Adv. Water. Resour.*, 40, 54–70, [doi:10.1016/j.advwatres.2012.01.009](https://doi.org/10.1016/j.advwatres.2012.01.009), 2012.
- Cesca, M. and D’Agostino, V.: Comparison between FLO-2D and RAMMS in debris-flow modelling: a case study in the Dolomites, *WIT Transactions on Engineering Sciences*, 60, 197–206, 2008.
- 520 Chen, H.-X., Li, J., Feng, S.-J., Gao, H.-Y., and Zhang, D.-M.: Simulation of interactions between debris flow and check dams on three-dimensional terrain, *Eng. Geol.*, 251, 48–62, [doi:10.1016/j.enggeo.2019.02.001](https://doi.org/10.1016/j.enggeo.2019.02.001), 2019.
- Choi, S.-K., Park, J.-Y., Lee, D.-H., Lee, S.-R., Kim, Y.-T., and Kwon, T.-H.: Assessment of barrier location effect on debris flow based on smoothed particle hydrodynamics (SPH) simulation on 3D terrains, *Landslides*, 18, 217–234, [doi:10.1007/s10346-020-01477-5](https://doi.org/10.1007/s10346-020-01477-5), 2021.
- 525 Dai, Z., Li, X., and Lan, B.: Three-dimensional modeling of tsunami waves triggered by submarine landslides based on the smoothed particle hydrodynamics method, *J. Mar. Sci. Eng.*, 11, 2015, [doi:10.3390/jmse11102015](https://doi.org/10.3390/jmse11102015), 2023.
- Dai, Z., Xie, J., Qin, S., and Chen, S.: Numerical Investigation of Surge Waves Generated by Submarine Debris Flows, *Water*, 13, 2276, [doi:10.3390/w13162276](https://doi.org/10.3390/w13162276), 2021.
- 530 de Lange, S. I., Santa, N., Pudasaini, S. P., Kleinhans, M. G., and de Haas, T.: Debris-flow generated tsunamis and their dependence on debris-flow dynamics, *Coast. Eng.*, 157, 103623, [doi:10.1016/j.coastaleng.2019.103623](https://doi.org/10.1016/j.coastaleng.2019.103623), 2020.
- Denlinger, R. P. and Iverson, R. M.: Flow of variably fluidized granular masses across three-dimensional terrain: 2. Numerical predictions and experimental tests, *J. Geophys. Res. Solid Earth*, 106, 553–566, [doi:10.1029/2000JB900330](https://doi.org/10.1029/2000JB900330), 2001.
- Franci, A., Cremonesi, M., Perego, U., Crosta, G., and Oñate, E.: 3D simulation of Vajont disaster. Part 1: Numerical formulation and validation, *Eng. Geol.*, 279, 105854, [doi:10.1016/j.enggeo.2020.105854](https://doi.org/10.1016/j.enggeo.2020.105854), 2020.
- 535 Franco, A., Moernaut, J., Schneider-Muntau, B., Strasser, M., and Gerns, B.: Triggers and consequences of landslide-induced impulse waves – 3D dynamic reconstruction of the Taan Fiord 2015 tsunami event, *Eng. Geol.*, 294, 106384, [doi:10.1016/j.enggeo.2021.106384](https://doi.org/10.1016/j.enggeo.2021.106384), 2021.
- Frank, F., McArdell, B. W., Huggel, C., and Vieli, A.: The importance of entrainment and bulking on debris flow runout modeling: examples from the Swiss Alps, *Nat. Hazards Earth Syst. Sci.*, 15, 2569–2583, [doi:10.5194/nhess-15-2569-2015](https://doi.org/10.5194/nhess-15-2569-2015), 2015.
- 540



- Fritz, H. M., Hager, W. H., and Minor, H. E.: Near Field Characteristics of Landslide Generated Impulse Waves, *J. Waterw. Port Coast. Ocean Eng.*, 130, 287–302, [doi:10.1061/\(ASCE\)0733-950X\(2004\)130:6\(287\)](https://doi.org/10.1061/(ASCE)0733-950X(2004)130:6(287)), 2004.
- Gao, Y., Yin, Y., Li, B., Feng, Z., Wang, W., Zhang, N., and Xing, A.: Characteristics and numerical runout modeling of the heavy rainfall-induced catastrophic landslide–debris flow at Sanxicun, Dujiangyan, China, following the Wenchuan Ms 8.0 earthquake, *Landslides*, 14, 1361–1374, [doi:10.1007/s10346-016-0793-4](https://doi.org/10.1007/s10346-016-0793-4), 2017.
- 545 Guan, X. and Shi, H.: Translational momentum of deformable submarine landslides off a slope, *J. Fluid. Mech.*, 960, A23, [doi:10.1017/jfm.2023.177](https://doi.org/10.1017/jfm.2023.177), 2023.
- Han, Z., Su, B., Li, Y., Dou, J., Wang, W., and Zhao, L.: Modeling the progressive entrainment of bed sediment by viscous debris flows using the three-dimensional SC-HBP-SPH method, *Water Res.*, 182, 116031, [doi:10.1016/j.watres.2020.116031](https://doi.org/10.1016/j.watres.2020.116031), 2020.
- 550 Heinrich, P.: Nonlinear Water Waves Generated by Submarine and Aerial Landslides, *J. Waterw. Port Coast. Ocean Eng.*, 118, 249–266, [doi:10.1061/\(ASCE\)0733-950X\(1992\)118:3\(249\)](https://doi.org/10.1061/(ASCE)0733-950X(1992)118:3(249)), 1992.
- Heller, V. and Hager Willi, H.: Impulse Product Parameter in Landslide Generated Impulse Waves, *J. Waterw. Port Coast. Ocean Eng.*, 136, 145–155, [doi:10.1061/\(ASCE\)WW.1943-5460.0000037](https://doi.org/10.1061/(ASCE)WW.1943-5460.0000037), 2010.
- 555 Heller, V. and Spinneken, J.: On the effect of the water body geometry on landslide–tsunamis: Physical insight from laboratory tests and 2D to 3D wave parameter transformation, *Coast. Eng.*, 104, 113–134, [doi:10.1016/j.coastaleng.2015.06.006](https://doi.org/10.1016/j.coastaleng.2015.06.006), 2015.
- Horton, P., Jaboyedoff, M., Rudaz, B., and Zimmermann, M.: Flow-R, a model for susceptibility mapping of debris flows and other gravitational hazards at a regional scale, *Nat. Hazards Earth Syst. Sci.*, 13, 869–885, [doi:10.5194/nhess-13-869-2013](https://doi.org/10.5194/nhess-13-869-2013), 2013.
- 560 Hungr, O., McDougall, S., and Bovis, M.: Entrainment of material by debris flows, in: *Debris-flow Hazards and Related Phenomena*, edited by: Jakob, M., and Hungr, O., Springer Berlin Heidelberg, Berlin, Heidelberg, 135–158, [doi:10.1007/3-540-27129-5_7](https://doi.org/10.1007/3-540-27129-5_7), 2005.
- Hürlimann, M., Abancó, C., Moya, J., and Vilajosana, I.: Results and experiences gathered at the Rebaixader debris-flow monitoring site, Central Pyrenees, Spain, *Landslides*, 11, 939–953, [doi:10.1007/s10346-013-0452-y](https://doi.org/10.1007/s10346-013-0452-y), 2014.
- 565 Hussin, H. Y., Quan Luna, B., van Westen, C. J., Christen, M., Malet, J. P., and van Asch, T. W. J.: Parameterization of a numerical 2-D debris flow model with entrainment: a case study of the Faucon catchment, Southern French Alps, *Nat. Hazards Earth Syst. Sci.*, 12, 3075–3090, [doi:10.5194/nhess-12-3075-2012](https://doi.org/10.5194/nhess-12-3075-2012), 2012.
- ICOLD, C.: Sedimentation and sustainable use of reservoir and river systems, Draft ICOLD Bull Sedimentation Committee, 570 2009.
- Imamura, F., Hashi, K., and Imteaz, M. A.: Modeling for Tsunamis Generated by Landsliding and Debris Flow, in: *Tsunami Research at the End of a Critical Decade*, edited by: Hebenstreit, G. T., Springer Netherlands, Dordrecht, 209–228, [doi:10.1007/978-94-017-3618-3_15](https://doi.org/10.1007/978-94-017-3618-3_15), 2001.
- Iverson, R. M., Reid, M. E., Logan, M., LaHusen, R. G., Godt, J. W., and Griswold, J. P.: Positive feedback and momentum growth during debris-flow entrainment of wet bed sediment, *Nat. Geosci.*, 4, 116–121, [doi:10.1038/ngeo1040](https://doi.org/10.1038/ngeo1040), 2011.
- 575 Kim, D.-H., Cho, Y.-S., and Kim, H.-J.: Well-Balanced Scheme between Flux and Source Terms for Computation of Shallow-Water Equations over Irregular Bathymetry, *J. Eng. Mech.*, 134, 277–290, [doi:10.1061/\(ASCE\)0733-9399\(2008\)134:4\(277\)](https://doi.org/10.1061/(ASCE)0733-9399(2008)134:4(277)), 2008.
- Kim, S. W., Chun, K. W., Kim, M., Catani, F., Choi, B., and Seo, J. I.: Effect of antecedent rainfall conditions and their variations on shallow landslide-triggering rainfall thresholds in South Korea, *Landslides*, 18, 569–582, [doi:10.1007/s10346-020-01505-4](https://doi.org/10.1007/s10346-020-01505-4), 2021.
- 580 Kim, Y., Byun, Y., Kim, Y., and Eo, Y.: Detection of *Cochlodinium polykrikoides* red tide based on two-stage filtering using



- MODIS data, *Desalin.*, 249, 1171–1179, [doi:10.1016/j.desal.2009.05.009](https://doi.org/10.1016/j.desal.2009.05.009), 2009.
- 585 Krvavica, N.: Re-evaluating efficiency of first-order numerical schemes for two-layer shallow water systems by considering different eigenvalue solutions, *Adv. Water. Resour.*, 137, 103508, [doi:10.1016/j.advwatres.2020.103508](https://doi.org/10.1016/j.advwatres.2020.103508), 2020.
- Lee, S., An, H., Kim, M., and Eu, S.: Preliminary analysis of nocturnal localized heavy rain-induced landslides in Yecheon County, Northern Gyeongsang Province, South Korea, *Landslides*, 21, 429–435, [doi:10.1007/s10346-023-02182-9](https://doi.org/10.1007/s10346-023-02182-9), 2024.
- Lee, S., An, H., Kim, M., and Kang, T.: Assessment of dam function deterioration due to landslide-debris flows: numerical modeling based on vegetation distribution scenarios, *Front. Earth. Sci.*, 11, 1216096, [doi:10.3389/feart.2023.1216096](https://doi.org/10.3389/feart.2023.1216096), 590 2023.
- Lee, S., An, H., Kim, M., Lee, G., and Shin, H.: Evaluation of different erosion–entrainment models in debris-flow simulation, *Landslides*, 19, 2075–2090, [doi:10.1007/s10346-022-01901-y](https://doi.org/10.1007/s10346-022-01901-y), 2022a.
- Lee, S., An, H., Kim, M., Lim, H., and Kim, Y.: A simple deposition model for debris flow simulation considering the erosion–entrainment–deposition process, *Remote Sens.*, 14, 1904, [doi:10.3390/rs14081904](https://doi.org/10.3390/rs14081904), 2022b.
- 595 Liang, Q. and Marche, F.: Numerical resolution of well-balanced shallow water equations with complex source terms, *Adv. Water. Resour.*, 32, 873–884, [doi:10.1016/j.advwatres.2009.02.010](https://doi.org/10.1016/j.advwatres.2009.02.010), 2009.
- Lyu, L., Xu, M., Wang, Z., Cui, Y., and Blanckaert, K.: A field investigation on debris flows in the incised Tongde sedimentary basin on the northeastern edge of the Tibetan Plateau, *Catena*, 208, 105727, [doi:10.1016/j.catena.2021.105727](https://doi.org/10.1016/j.catena.2021.105727), 2022.
- 600 Ma, S., Shao, X., and Xu, C.: Characterizing the Distribution Pattern and a Physically Based Susceptibility Assessment of Shallow Landslides Triggered by the 2019 Heavy Rainfall Event in Longchuan County, Guangdong Province, China, *Remote Sens.*, 14, 4257, [doi:10.3390/rs14174257](https://doi.org/10.3390/rs14174257), 2022.
- Mergili, M., Jaboyedoff, M., Pullarello, J., and Pudasaini, S. P.: Back calculation of the 2017 Piz Cengalo–Bondo landslide cascade with r.avaflow: what we can do and what we can learn, *Nat. Hazards Earth Syst. Sci.*, 20, 505–520, [doi:10.5194/nhess-20-505-2020](https://doi.org/10.5194/nhess-20-505-2020), 2020.
- 605 Mulligan, R. P. and Take, W. A.: On the transfer of momentum from a granular landslide to a water wave, *Coast. Eng.*, 125, 16–22, [doi:10.1016/j.coastaleng.2017.04.001](https://doi.org/10.1016/j.coastaleng.2017.04.001), 2017.
- Oguchi, T. and Oguchi, C. T.: Late Quaternary rapid talus dissection and debris flow deposition on an alluvial fan in Syria, *Catena*, 55, 125–140, [doi:10.1016/S0341-8162\(03\)00112-7](https://doi.org/10.1016/S0341-8162(03)00112-7), 2004.
- Pirulli, M. and Sorbino, G.: Assessing potential debris flow runout: a comparison of two simulation models, *Nat. Hazards Earth Syst. Sci.*, 8, 961–971, [doi:10.5194/nhess-8-961-2008](https://doi.org/10.5194/nhess-8-961-2008), 2008.
- 610 Pitman, E. B., Nichita, C. C., Patra, A., Bauer, A., Sheridan, M., and Bursik, M.: Computing granular avalanches and landslides, *Phys. Fluids*, 15, 3638–3646, [doi:10.1063/1.1614253](https://doi.org/10.1063/1.1614253), 2003.
- Pudasaini, S. P.: Dynamics of submarine debris flow and tsunami, *Acta. Mech.*, 225, 2423–2434, [doi:10.1007/s00707-014-1126-0](https://doi.org/10.1007/s00707-014-1126-0), 2014.
- 615 Pudasaini, S. P. and Krautblatter, M.: The mechanics of landslide mobility with erosion, *Nat. Commun.*, 12, 6793, [doi:10.1038/s41467-021-26959-5](https://doi.org/10.1038/s41467-021-26959-5), 2021.
- Pudasaini, S. P. and Mergili, M.: A Multi-Phase Mass Flow Model, *J. Geophys. Res. Earth Surf.*, 124, 2920–2942, [doi:10.1029/2019JF005204](https://doi.org/10.1029/2019JF005204), 2019.
- Qiu, H., Zhu, Y., Zhou, W., Sun, H., He, J., and Liu, Z.: Influence of DEM resolution on landslide simulation performance based on the Scoops3D model, *Geomat. Nat. Hazards Risk*, 13, 1663–1681, [doi:10.1080/19475705.2022.2097451](https://doi.org/10.1080/19475705.2022.2097451), 2022.
- 620 Rzdakiewicz, S. A., Mariotti, C., and Heinrich, P.: Numerical Simulation of Submarine Landslides and Their Hydraulic Effects, *J. Waterw. Port Coast. Ocean Eng.*, 123, 149–157, [doi:10.1061/\(ASCE\)0733-950X\(1997\)123:4\(149\)](https://doi.org/10.1061/(ASCE)0733-950X(1997)123:4(149)), 1997.



- Schnitter, G. and Weber, E.: Die Katastrophe von Vaiont in Oberitalien, 1964.
- Shaffer, J. A. and Parks, D. S.: Seasonal Variations in and Observations of Landslide Impacts on the Algal Composition of a
625 Puget Sound Nearshore Kelp Forest, *Bot. Mar.*, 37, 315–324, [doi:10.1515/botm.1994.37.4.315](https://doi.org/10.1515/botm.1994.37.4.315), 1994.
- Shen, W., Wang, D., Qu, H., and Li, T.: The effect of check dams on the dynamic and bed entrainment processes of debris
flows, *Landslides*, 16, 2201–2217, [doi:10.1007/s10346-019-01230-7](https://doi.org/10.1007/s10346-019-01230-7), 2019.
- Shrestha, B. B., Nakagawa, H., Kawaike, K., Baba, Y., and Zhang, H.: Driftwood deposition from debris flows at slit-check
dams and fans, *Nat. Hazards*, 61, 577–602, [doi:10.1007/s11069-011-9939-9](https://doi.org/10.1007/s11069-011-9939-9), 2012.
- 630 Shugar, D. H., Jacquemart, M., Shean, D., Bhushan, S., Upadhyay, K., Sattar, A., Schwanghart, W., McBride, S., de Vries, M.
V. W., Mergili, M., Emmer, A., Deschamps-Berger, C., McDonnell, M., Bhambri, R., Allen, S., Berthier, E., Carrivick, J.
L., Clague, J. J., Dokukin, M., Dunning, S. A., Frey, H., Gascoin, S., Haritashya, U. K., Huggel, C., Kääb, A., Kargel, J.
S., Kavanaugh, J. L., Lacroix, P., Petley, D., Rupper, S., Azam, M. F., Cook, S. J., Dimri, A. P., Eriksson, M., Farinotti,
D., Fiddes, J., Gnyawali, K. R., Harrison, S., Jha, M., Koppes, M., Kumar, A., Leinss, S., Majeed, U., Mal, S., Muhuri,
635 A., Noetzli, J., Paul, F., Rashid, I., Sain, K., Steiner, J., Ugalde, F., Watson, C. S., and Westoby, M. J.: A massive rock and
ice avalanche caused the 2021 disaster at Chamoli, Indian Himalaya, *Sci.*, 373, 300–306, [doi:10.1126/science.abh4455](https://doi.org/10.1126/science.abh4455),
2021.
- Slingerland, R. L. and Voight, B.: Chapter 9 - Occurrences, Properties, and Predictive Models of Landslide-Generated Water
Waves, in: *Developments in Geotechnical Engineering*, edited by: Voight, B., Elsevier, 317–394, [doi:10.1016/B978-0-444-41508-0.50017-X](https://doi.org/10.1016/B978-0-444-41508-0.50017-X), 1979.
640
- Stolz, A. and Huggel, C.: Debris flows in the Swiss National Park: the influence of different flow models and varying DEM
grid size on modeling results, *Landslides*, 5, 311–319, [doi:10.1007/s10346-008-0125-4](https://doi.org/10.1007/s10346-008-0125-4), 2008.
- Takahashi, T.: Mechanical Characteristics of Debris Flow, *J. Hydraul. Div.*, 104, 1153–1169, [doi:10.1061/JYCEAJ.0005046](https://doi.org/10.1061/JYCEAJ.0005046),
1978.
- 645 Terzaghi, K.: Mechanism of Landslides, in: *Application of Geology to Engineering Practice, Berkey Volume ed.*, edited by:
Paige, S., Geological Society of America, New York, 83–123, [doi:10.1130/Berkey.1950.83](https://doi.org/10.1130/Berkey.1950.83), 1950.
- VanDine, D. F. and Bovis, M.: History and Goals of Canadian Debris Flow Research, A Review, *Nat. Hazards*, 26, 67–80,
[doi:10.1023/A:1015220811211](https://doi.org/10.1023/A:1015220811211), 2002.
- Voellmy, A.: Über die Zerstörungskraft von Lawinen, *Bauztg.*, 73, 159–165, 1955.
- 650 Wang, F.-W., Zhang, Y.-M., Huo, Z.-T., Matsumoto, T., and Huang, B.-L.: The July 14, 2003 Qianjiangping landslide, Three
Gorges Reservoir, China, *Landslides*, 1, 157–162, [doi:10.1007/s10346-004-0020-6](https://doi.org/10.1007/s10346-004-0020-6), 2004.
- Wieczorek, G. F.: Landslides: investigation and mitigation., in: *Transp. Res. Board Spec. Rep.*, edited by: Turner, A. K., and
Schuster, R. L., 247, Washington D.C., 76–90, 1996.
- Wieczorek, G. F. and Glade, T.: Climatic factors influencing occurrence of debris flows, in: *Debris-flow Hazards and Related
655 Phenomena*, edited by: Jakob, M., and Hungr, O., Springer Berlin Heidelberg, Berlin, Heidelberg, 325–362,
[doi:10.1007/3-540-27129-5_14](https://doi.org/10.1007/3-540-27129-5_14), 2005.
- Zhao, Y., Meng, X., Qi, T., Li, Y., Chen, G., Yue, D., and Qing, F.: AI-based rainfall prediction model for debris flows, *Eng.
Geol.*, 296, 106456, [doi:10.1016/j.enggeo.2021.106456](https://doi.org/10.1016/j.enggeo.2021.106456), 2022.
- Zhou, G. G. D., Li, S., Song, D., Choi, C. E., and Chen, X.: Depositional mechanisms and morphology of debris flow: physical
660 modelling, *Landslides*, 16, 315–332, [doi:10.1007/s10346-018-1095-9](https://doi.org/10.1007/s10346-018-1095-9), 2019.



Table 1. Input data and parameters setting for numerical models used in this study.

Model	Input data		Value	Unit
Topography	Initial zone		1.0	[m]
	Soil depth		1.0	[m]
Water	Water level		119	[m]
	Density	ρ_w	1000	[kg · m ⁻³]
	Manning coefficient	n	0.01	[-]
Debris flow	Voellmy rheology	μ	0.05	[-]
		ζ	500	[m · s ⁻²]
	Erosion-entrainment- deposition mechanism	dz/dt_e	0.05	[m · s ⁻¹]
		dz/dt_d	0.01	[m · s ⁻¹]
		$dz/d\tau$	0.2	[m · kPa ⁻¹]
		ρ_d	1900	[kg · m ⁻³]
		τ_e	1.0	[kPa]
		τ_d	0.5	[kPa]
		Interaction friction coefficient	f^{int}	10.0



665

Table 2. Simulation results for each criterion according to changes in Voellmy rheology parameters and interface friction coefficient f^{int} change.

Parameters		Debris flow			Water		
μ	ζ (m/s ²)	Maximum flow height ¹ (m)	Maximum velocity ¹ (m/s)	Maximum momentum ¹ (ton·m/s)	Underwater flow distance ² (m)	Amplitude of the first wave ³ (m)	Maximum crest amplitude (m)
0.030	500	7.02	3.56	17.58	183	1.420	1.883
0.035		6.44	3.54	13.37	148	1.160	1.481
0.040		5.78	3.22	9.42	117	0.881	1.093
0.045		4.94	2.51	5.73	84	0.584	0.702
0.050	500	3.52	1.09	2.06	44	0.231	0.327
0.050	400	3.27	1.18	1.88	46	0.221	0.336
	800	4.31	1.90	3.04	61	0.284	0.477
	1000	4.33	1.74	2.74	59	0.237	0.440
	2000	5.08	2.06	3.83	68	0.420	0.593

¹ Observed near the reservoir (1,378 m)
² Measured from the point where the water meets the ground (1,379 m)
³ Observed in p1, Fig. 6 (1,450 m)



Table 3. R^2 analysis results between debris flow characteristics and waves caused by debris flow during flood level and high water level seasons.

Dependent variable	Independent variable	a^*	R^2
Maximum flow height	Underwater flow distance	21.704	0.862
	Amplitude of the first wave	0.142	0.837
	Maximum crest amplitude	0.203	0.802
Maximum velocity	Underwater flow distance	26.921	0.842
	Amplitude of the first wave	0.173	0.787
	Maximum crest amplitude	0.253	0.790
Maximum momentum	Underwater flow distance	12.279	0.964
	Amplitude of the first wave	0.083	0.985
	Maximum crest amplitude	0.120	0.983

* $y=a \times x$



Table 4. R^2 and RMSE analysis results between debris flow characteristics and waves caused by debris flow for two cases: high-water and flood level.

Dependent variable	Independent variable	High water level		Flood level	
		R^2	RMSE (m)	R^2	RMSE (m)
Maximum flow height	Underwater flow distance	0.953	38.006	0.872	30.754
	Amplitude of the first wave	0.812	0.207	0.870	0.286
	Maximum crest amplitude	0.872	0.442	0.883	0.361
Maximum velocity	Underwater flow distance	0.573	38.514	0.892	35.495
	Amplitude of the first wave	0.807	0.235	0.893	0.331
	Maximum crest amplitude	0.606	0.450	0.870	0.377
Maximum momentum	Underwater flow distance	0.958	13.071	0.996	20.982
	Amplitude of the first wave	0.971	0.073	0.989	0.076
	Maximum crest amplitude	0.990	0.109	0.994	0.126

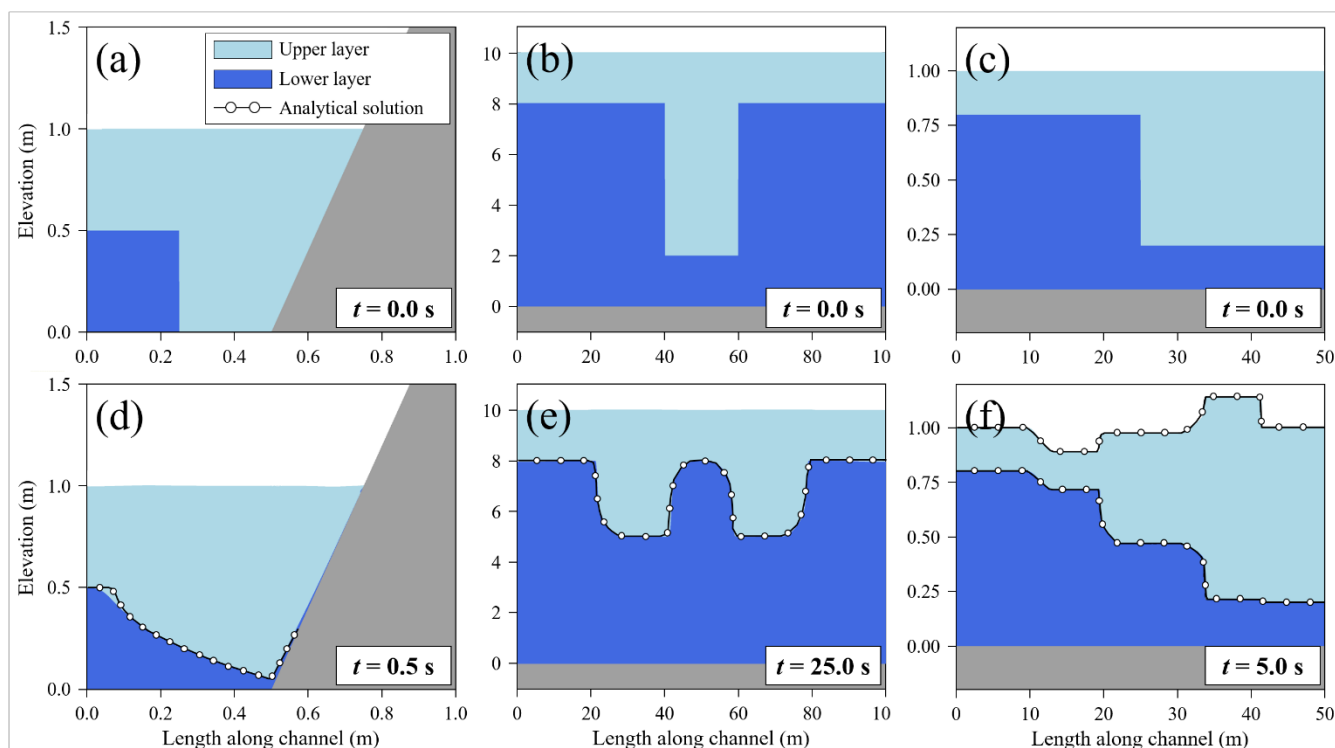
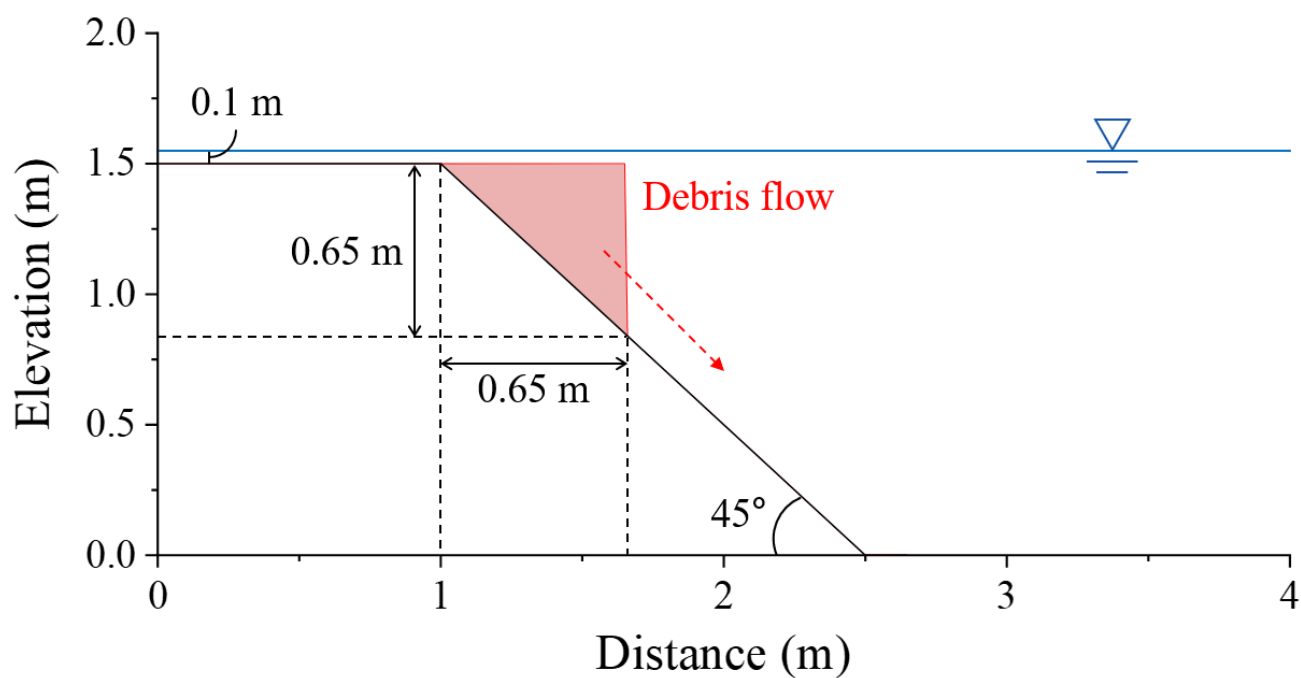


Figure 1. Numerical tests: (a, d) Bouchut and Zeitlin (2010), (b, e) Krvavica's (2020) Test II and (c, f) Krvavica's (2020) Test IV.



680

Figure 2. Overview of the Rzadkiewicz et al.'s (1997) experiment setup.

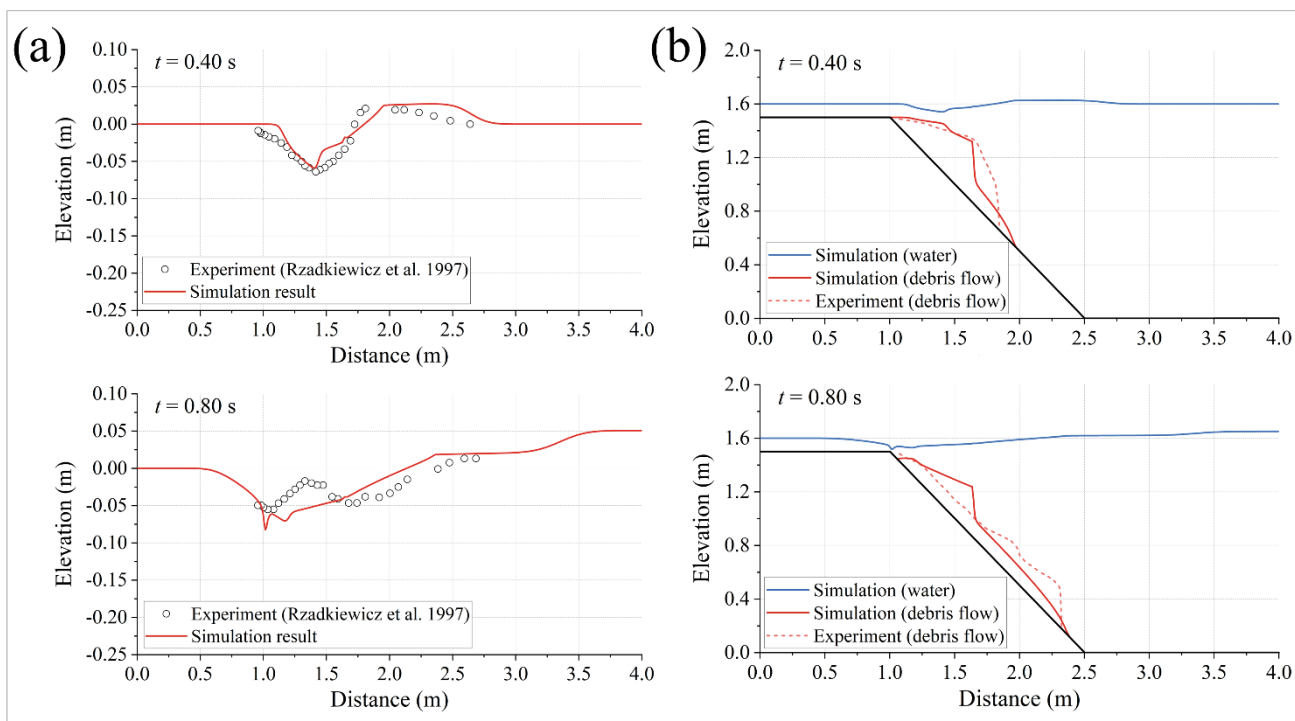


Figure 3. Comparison between the simulated and Rzadkiewicz et al.'s (1997) experimental waves at 0.40 s and 0.80 s: (a)

685 water surface and (b) combined water surface and debris flow thickness.

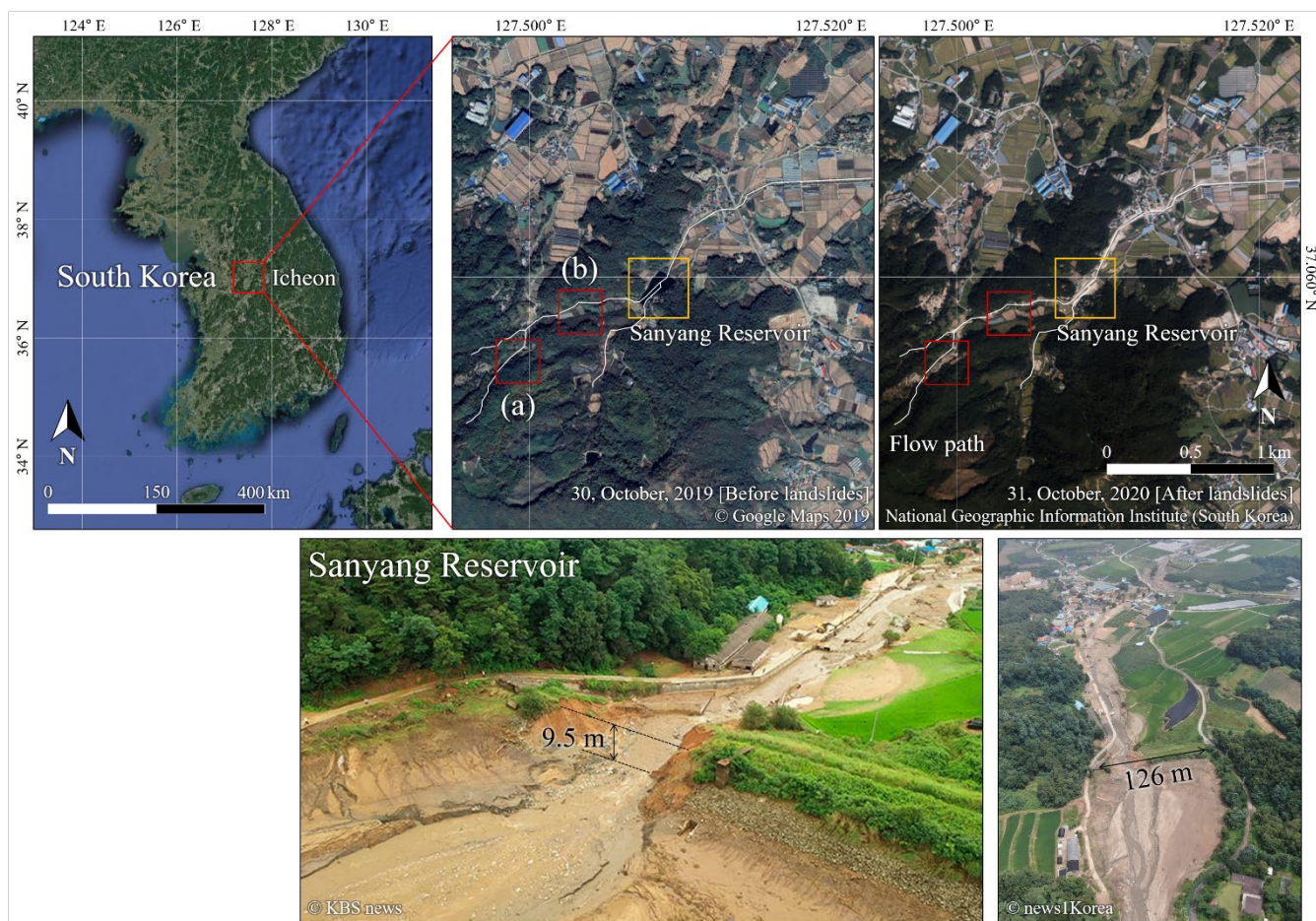


Figure 4. Study area and events: 2020 Sanyang Reservoir collapse event at Icheon in South Korea; (a) and (b) evidence of landslides and debris flows (from © Google Maps 2019, National Geographic Information Institute of South Korea, © KBS news, and © news1Korea).

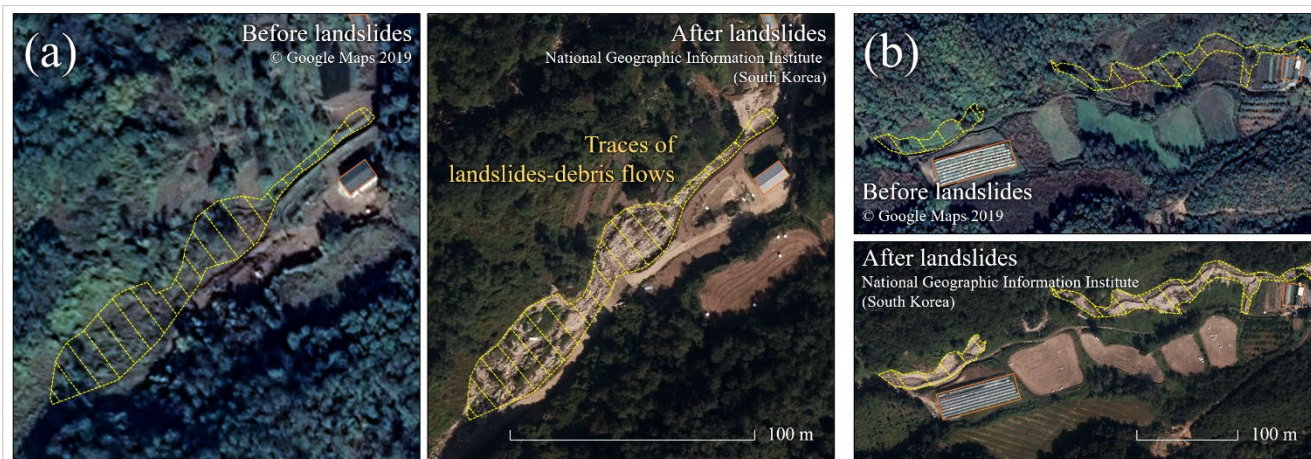


Figure 5. Evidence of landslides and debris flows occurred (from © Google Maps 2019 and National Geographic Information Institute of South Korea).

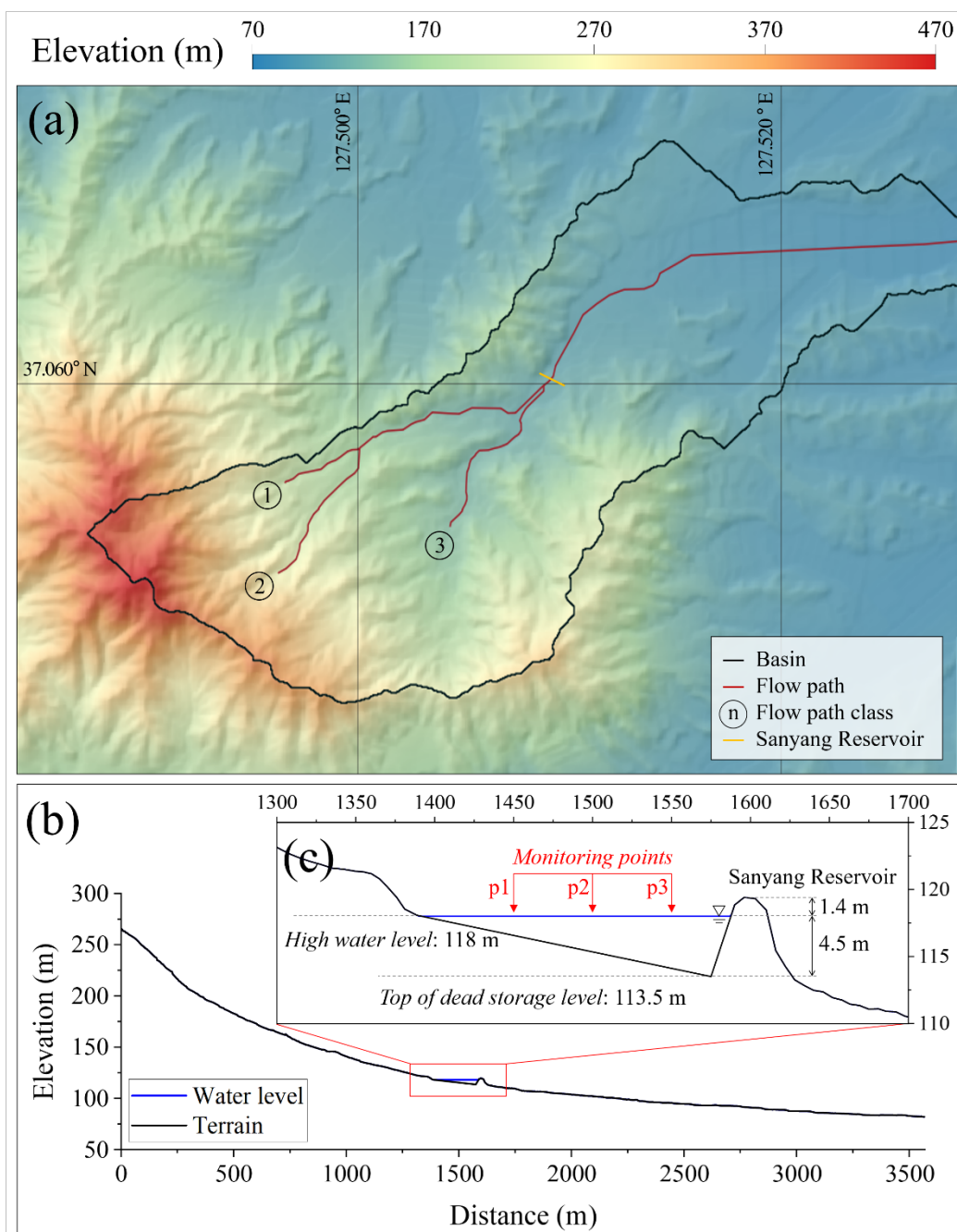
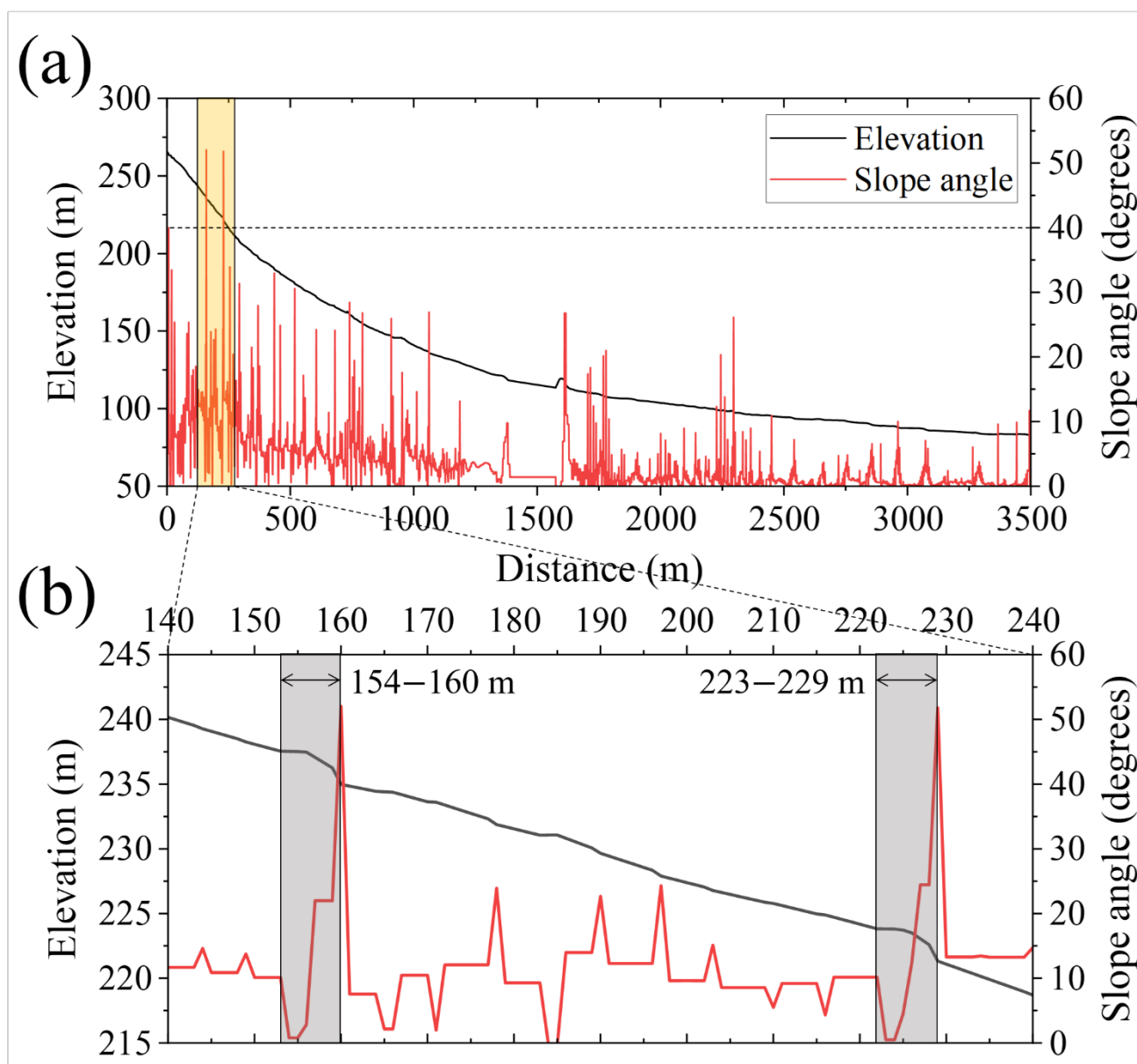


Figure 6. Topography data of Sanyang Reservoir basin: (a) DEM, (b) cross-section of the flow path 2, (c) cross-section near the Sanyang Reservoir.



700 **Figure 7.** Slope at each point: (a) all sections, (b) sections with slopes greater than 40°.

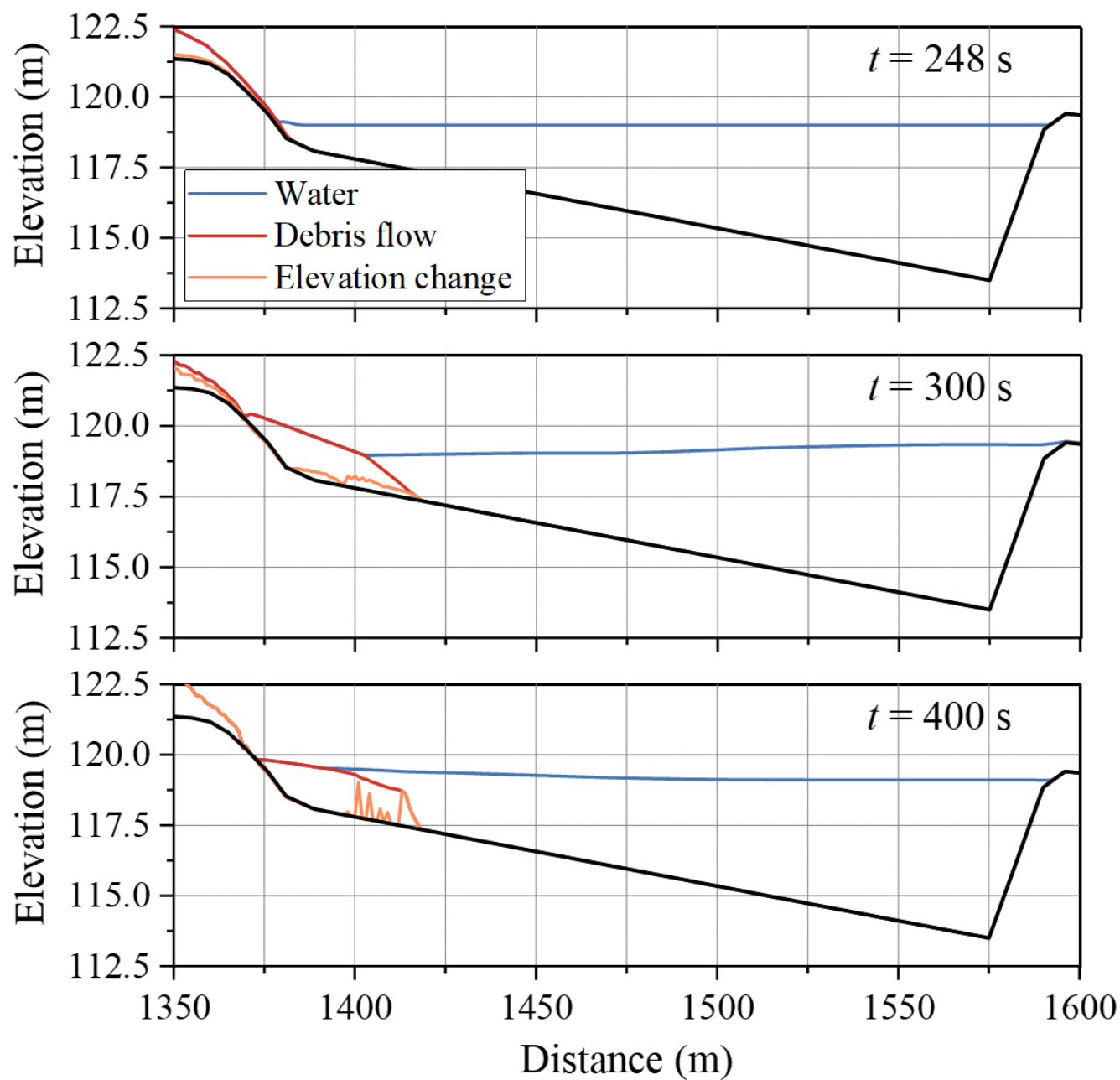


Figure 8. Simulation results for debris flow into the reservoir over time.

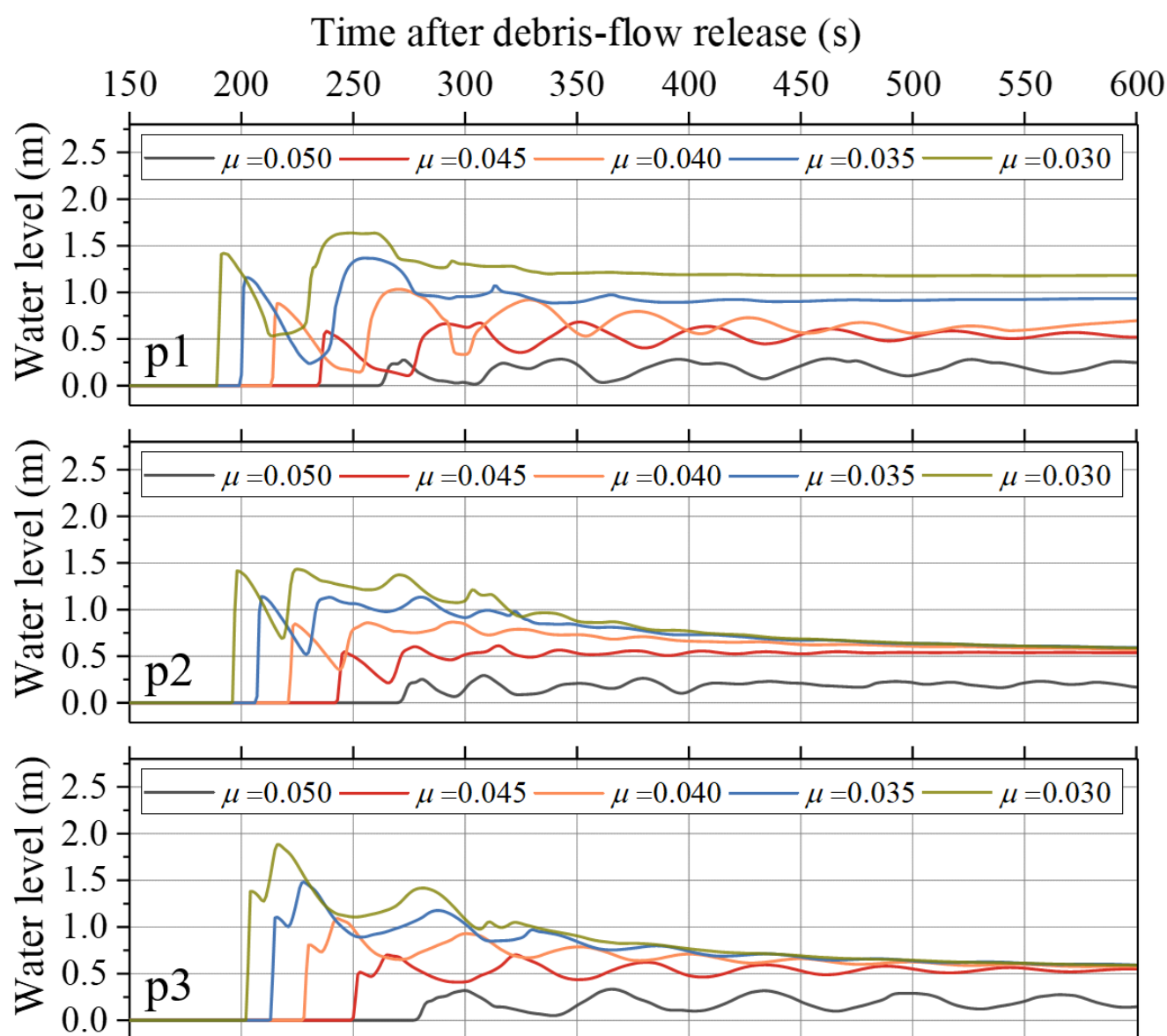


Figure 9. Water surface elevation profiles over time at p1, p2, and p3 for each Voellmy rheology parameters μ indicating the differences in wave amplitude and wave speed.

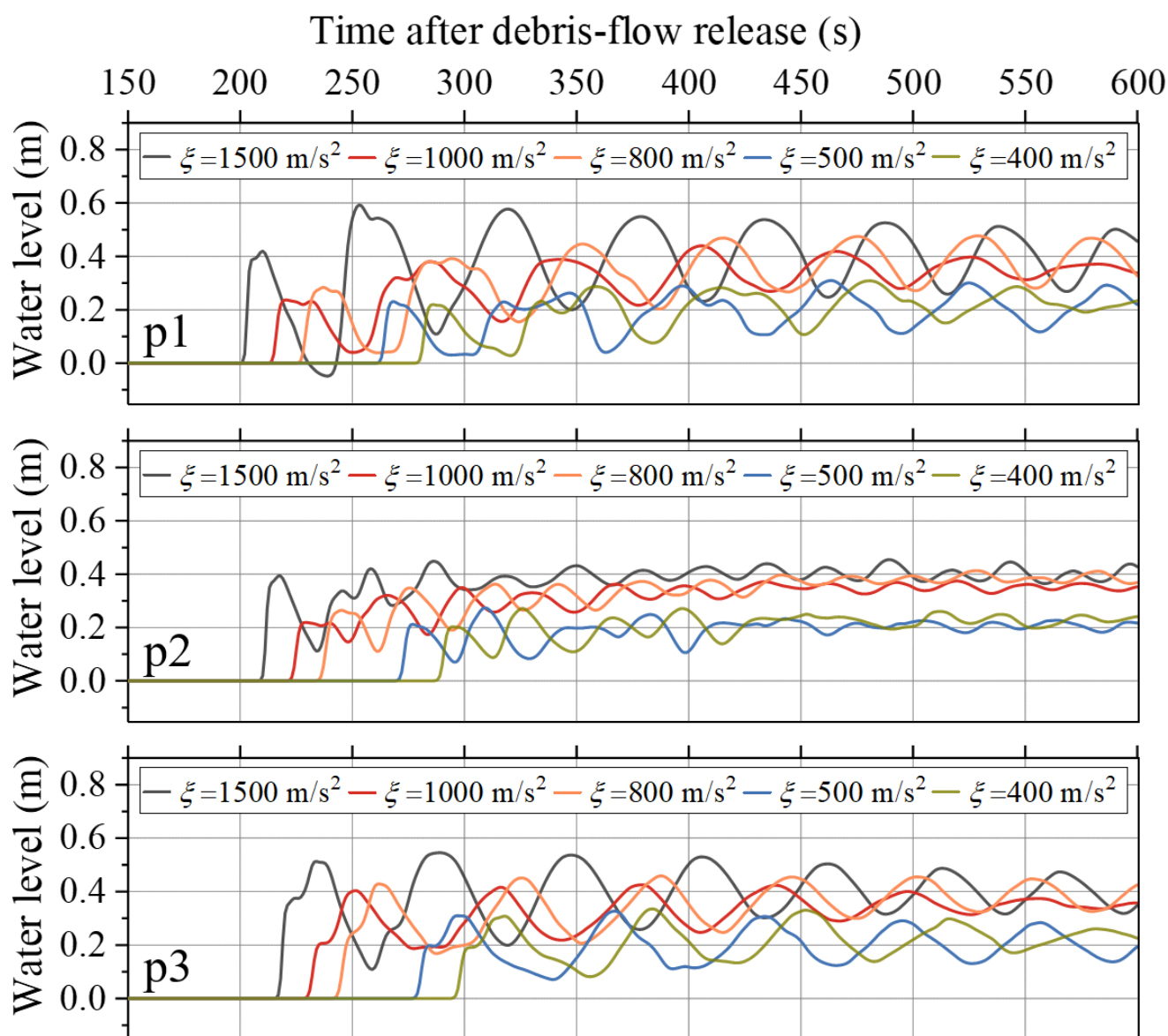
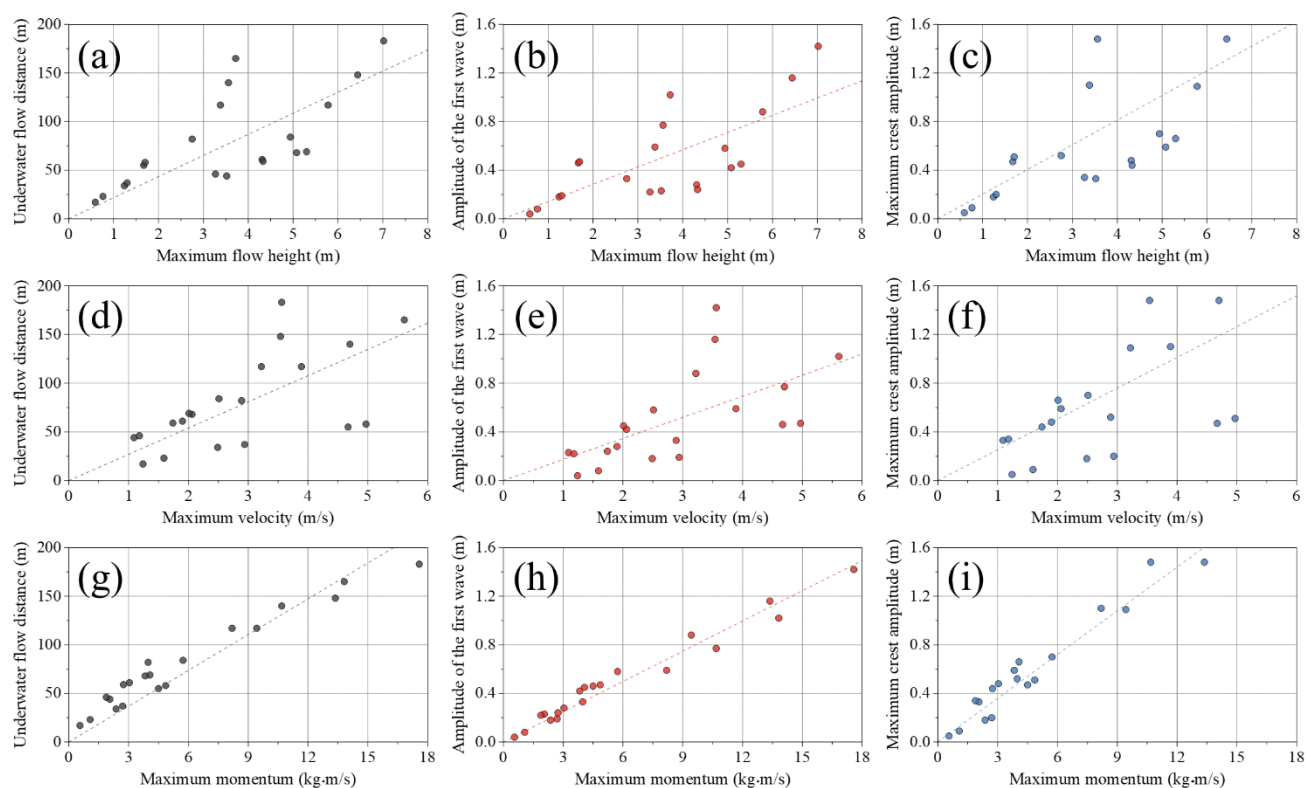


Figure 10. Water surface elevation profiles over time at p1, p2, and p3 for each Voellmy rheology parameters ξ indicating the differences in wave amplitude and wave speed.



715 **Figure 11.** Correlation between debris flow characteristics and waves caused by debris flow during flood level and seasons of high-water level.

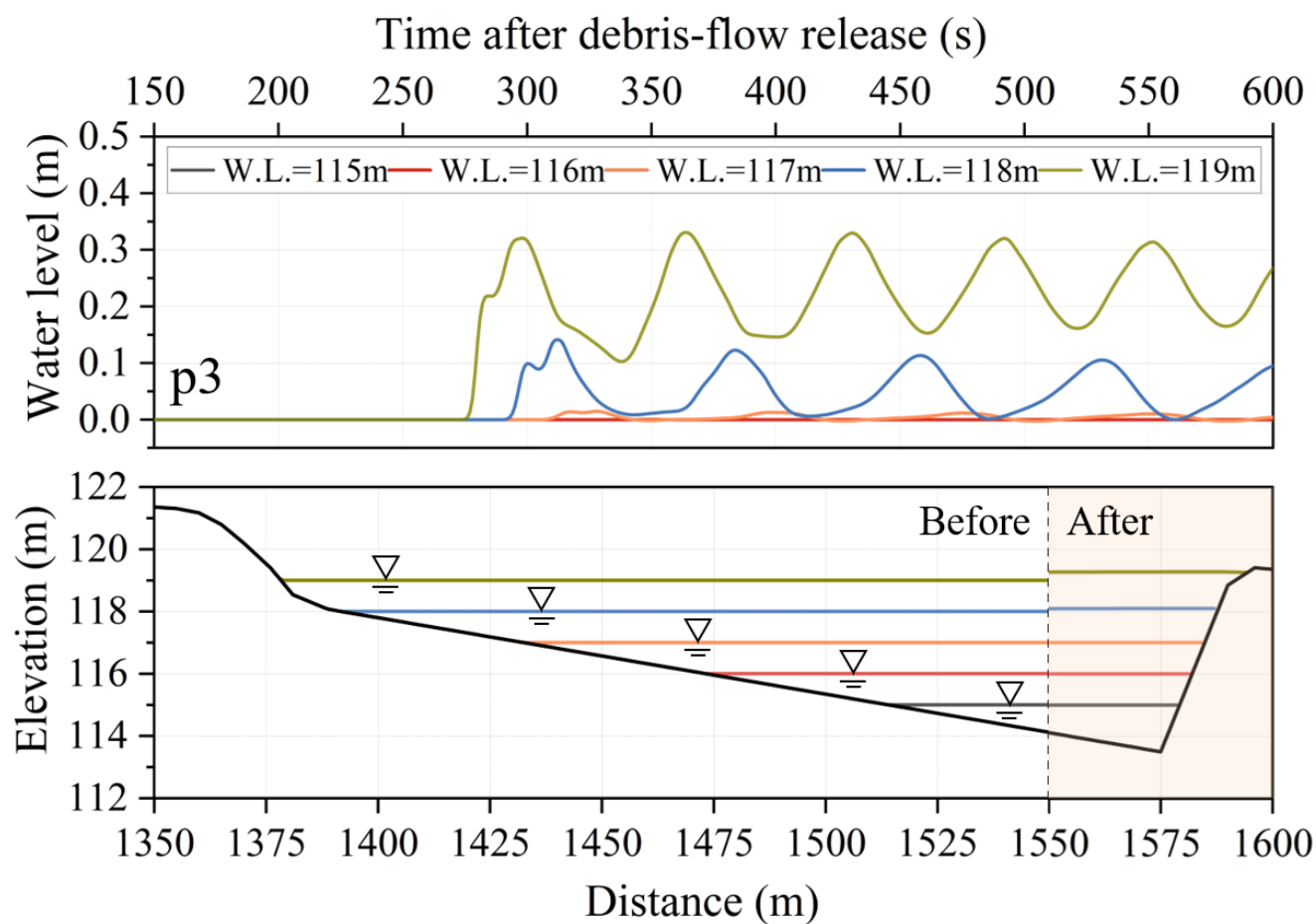


Figure 12. Water surface elevation profiles over time at p3 and reservoir level change for reservoir level.